AGU PUBLICATIONS

JGR

Journal of Geophysical Research: Solid Earth

RESEARCH ARTICLE

10.1002/2013JB010796

Key Points:
- Mainshocks at Qeshm and Fin ruptured the middle sedimentary cover
- Deep aftershocks may reflect straining of Hormuz rocks in response to main shock
- Most large earthquakes in the Zagros are in the cover, not the basement

Correspondence to:
E. Nissen,
enissen@mines.edu

Citation:
Nissen, E., J. Jackson, S. Jahani, and M. Tatar (2014), Zagros "phantom earthquakes" reassessed—The interplay of seismicity and deep salt flow in the Simply Folded Belt?, *J. Geophys. Res. Solid Earth*, *119*, doi:10.1002/2013JB010796.

Received 25 OCT 2013
Accepted 12 FEB 2014
Accepted article online 26 FEB 2014

Zagros "phantom earthquakes" reassessed—The interplay of seismicity and deep salt flow in the Simply Folded Belt?

Edwin Nissen[1], James Jackson[2], Salman Jahani[3], and Mohammad Tatar[4]

[1]Department of Geophysics, Colorado School of Mines, Golden, Colorado, USA, [2]COMET+, Bullard Laboratories, Department of Earth Sciences, University of Cambridge, Cambridge, UK, [3]National Iranian Oil Company, Tehran, Iran, [4]International Institute of Earthquake Engineering and Seismology, Tehran, Iran

Abstract Unraveling the contributions of main shock slip, aftershocks, aseismic afterslip, and postseismic relaxation to the deformation observed in earthquake sequences heightens our understanding of crustal rheology, triggering phenomena, and seismic hazard. Here, we revisit two recent earthquakes in the Zagros mountains (Iran) which exhibited unusual and contentious aftereffects. The M_w ~6 earthquakes at Qeshm (2005) and Fin (2006) are both associated with large interferometric synthetic aperture radar (InSAR) signals, consistent with slip on steep reverse faults in carbonate rocks of the middle sedimentary cover, but small aftershocks detected with local seismic networks were concentrated at significantly greater depths. This discrepancy can be interpreted in one of two ways: either (1) there is a genuine vertical separation between main shock and aftershocks, reflecting a complex stress state near the basement-cover interface, or (2) the aftershocks delimit the main shock slip and the InSAR signals were caused by shallow, updip afterslip (phantom earthquakes) with very similar magnitudes, mechanisms, and geographical positions as the original earthquakes. Here, we show that main shock centroid depths obtained from body waveform modeling—which in this instance is the only method that can reveal for certain the depth at which seismic slip was centered—strongly support the first interpretation. At Qeshm, microseismic aftershock depths are centered at the level of the Hormuz Formation, an Infracambrian sequence of intercalated evaporitic and nonevaporitic sediments. These aftershocks may reflect the breaking up of harder Hormuz sediments and adjacent strata as the salt flows in response to main shock strain at the base of the cover. This work bolsters recent suggestions that most large earthquakes in the Zagros are contained within carbonate rocks in the midlower sedimentary cover and that the crystalline basement shortens mostly aseismically.

1. Introduction

The advent of spaceborne interferometric synthetic aperture radar (InSAR) in the 1990s equipped geologists with the means to detect Earth surface deformation over wide regions with unparalleled spatial resolution and precision. Its capability for mapping coseismic displacements and resolving these into patterns of fault slip is well documented, and InSAR-derived source models are fast becoming routine for large, continental earthquakes [*Weston et al.*, 2011, 2012; *Wright et al.*, 2013]. InSAR has also been instrumental in imaging subtle postseismic deformation signals—including afterslip, viscoelastic relaxation, and poroelastic rebound [e.g., *Massonnet et al.*, 1994; *Peltzer et al.*, 1996; *Deng et al.*, 1998]—as well as fault creep and interseismic strain accumulation [e.g., *Bürgmann et al.*, 1998; *Wright et al.*, 2001], leading to a surge of new insights into continental tectonics, rheology, and seismic hazard.

Unfortunately, the approximately monthly repeat time between successive SAR satellite orbits over a given area severely limits our ability to distinguish coseismic slip from triggered postseismic deformation using InSAR alone. One way in which these effects could potentially be unraveled is by integrating seismological source observations. By modeling teleseismic body waveforms whose wavelengths are long compared to the causative faulting, a point source ("centroid") earthquake source solution can be obtained, comprising a focal mechanism, a simplified slip history (the "source time function"), and a centroid depth which represents the weighted average depth of seismic slip [e.g., *Molnar and Lyon-Caen*, 1989]. If the seismic and aseismic contributions to the geodetic surface deformation involve different source mechanisms or occur at different depths, it should therefore be possible to distinguish them by integrating InSAR and body waveform analyses.

In this paper, we use this approach to reassess a pair of unusual earthquake sequences in the Zagros fold-and-thrust belt of Iran. The M_w ~6 main shocks, at Qeshm Island in 2005 and Fin in 2006, are both associated

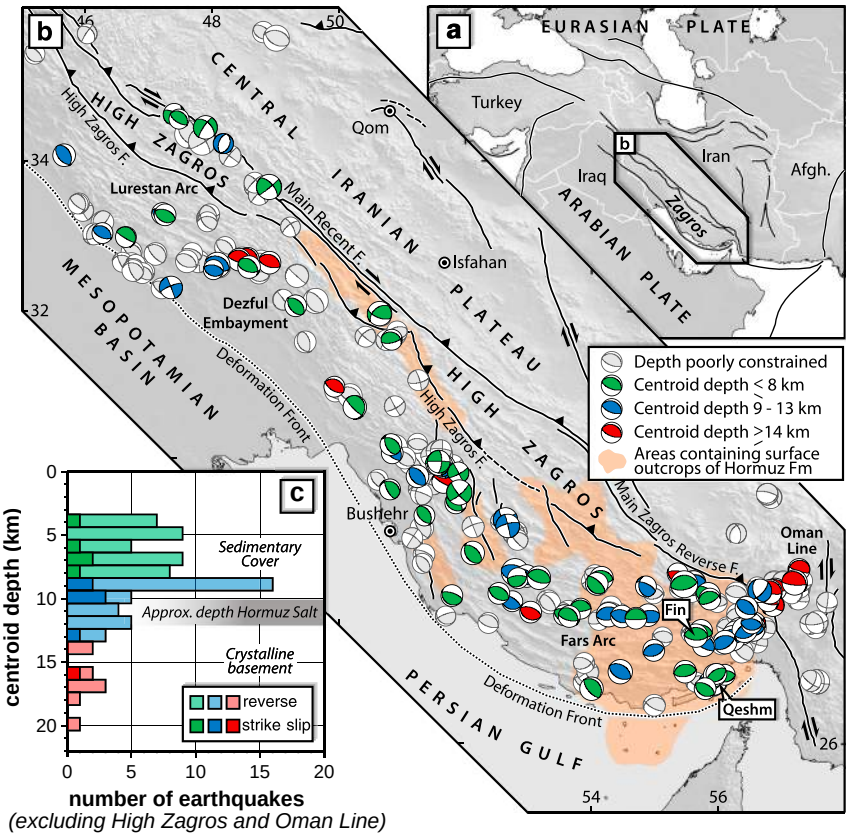

Figure 1. (a) Location of the Zagros mountains within the Arabia-Eurasian collision zone. (b) Teleseismic earthquake focal mechanisms in the Zagros, as detailed in *Nissen et al.* [2011] but updated through 2012. Light grey focal spheres are those without well-constrained depths; most of these are Global Centroid Moment Tensor (GCMT) mechanisms whose body waveforms were too noisy to model accurately. Green focal spheres are those with centroid depths of 4–8 km, constrained by body waveform modeling; within the SFB, these are unequivocally within the cover. Blue focal spheres are those with centroid depths of 9–13 km, which may have ruptured the cover, basement, or both. Red focal spheres are those with centroid depths of ≥14 km that in most places correspond to the basement. Areas which contain surface exposures of Hormuz salt are shaded in orange. (c) Centroid depth distribution of teleseismic body waveform models from within the Simply Folded Belt. Colors are as for Figure 1b; dark shades show strike-slip earthquakes, while light shades show reverse faulting events. We exclude from this histogram earthquakes along the Oman Line that occur NE of the surface exposure of the Main Zagros Reverse Fault, as well as those in the structurally distinct High Zagros.

with clear InSAR signals consistent with slip at shallow depths, but aftershock microseismicity—detected by local networks of seismometers deployed soon after the initial earthquakes—occurred at significantly greater depths. We begin by outlining the tectonic setting (section 2) before summarizing previous work on these earthquakes (section 3). Next, we present seismic reflection profiles that provide important new constraints on the subsurface structure of Qeshm Island (section 4). We then use InSAR modeling (section 5) together with long-period body waveform analyses (section 6) to determine whether (1) the main shock and aftershocks are vertically separated, as was originally suggested [*Nissen et al.*, 2010; *Roustaei et al.*, 2010], or (2) the aftershocks cluster around the main shock rupture, with a large, shallow pulse of aseismic slip (a "phantom earthquake") generating the surface deformation signals imaged by InSAR [*Barnhart and Lohman*, 2013; *Barnhart et al.*, 2013]. These competing interpretations have very different implications for the large-scale mechanics of the Zagros, including the role of salt, as well as for the appropriateness of using aftershock patterns to map main shock rupture extents.

2. Tectonic Setting

The Zagros mountains of Iran are amongst the world's most active continental earthquake belts and have profoundly influenced our understanding of fold-and-thrust mechanics and salt tectonics. The range forms the leading edge of the collision between the Arabian and Eurasian continental plates (Figure 1a), which

probably started in the late Eocene or early Oligocene [*Allen and Armstrong*, 2008; *Mouthereau et al.*, 2012; *McQuarrie and van Hinsbergen*, 2013]. Today, the ~5–10 mm/yr of active shortening measured by GPS is concentrated within the lower elevation, southern/southwestern parts of the Zagros, known as the Simply Folded Belt (SFB) [*Hessami et al.*, 2006; *Walpersdorf et al.*, 2006]. The SFB is often delineated along strike into four domains: from NW to SE, the Kirkuk Embayment, the Lurestan (or Pusht-e-Kuh) Arc, the Dezful Embayment, and the broad Fars Arc on which this paper focuses. The SFB is separated from the structurally distinct and largely inactive High Zagros by the High Zagros Fault, a major NE-dipping thrust (Figure 1b).

2.1. Salt, Stratigraphy, and Cover Thickness

The SFB contains a thick, folded pile of sediments which span the entire Phanerozoic. In much of the Fars Arc and along the High Zagros Fault, these sediments are detached from underlying basement rocks by the late Precambrian-Cambrian Hormuz Formation, an interbedded succession of evaporitic and nonevaporitic sediments which reaches the surface in numerous salt diapirs, many of which are still active (Figure 1b) [*Gansser*, 1960; *Kent*, 1970, 1979; *Ala*, 1974; *Edgell*, 1996; *Jahani et al.*, 2007; *Barnhart and Lohman*, 2012]. It is not clear whether the Hormuz Fm extends into the northwestern SFB, although if it is absent there it is probably replaced by another weak, detachment-forming horizon [*Sherkati and Letouzey*, 2004; *Carruba et al.*, 2006].

The Hormuz salt is predominantly halite with some gypsum and anhydrite, while the nonevaporitic Hormuz sediments include a widespread black dolomite which gives many salt plugs their distinctive dark coloration, as well as limestones, shales, sandstones, conglomerates, and volcanic tuffs [*Gansser*, 1960; *Kent*, 1970, 1979]. Harder sediments have been dismantled by diapirism and tectonic folding and carried to the surface by salt flow, occasionally within large, intact rafts up to 2–4 km in diameter. Some diapirs also entrain rare specimens of igneous and metamorphic basement rocks which are thought to have been "plucked" from the floor of the Hormuz stratum. Speculative estimates of the original thickness of the Hormuz Fm range between ~1 km and ~4 km [see *Jahani et al.*, 2007]. Huge quantities of salt have since been extruded and removed by erosion, so in situ Hormuz rocks are probably considerably thinner than this at present. Indeed, the salt may have disappeared altogether in some places, welding the overlying Paleozoic sediments onto the basement. A few offshore seismic reflection lines from the eastern Persian Gulf provide the only published images of the Hormuz salt in its true stratigraphic position [*Jahani*, 2008; *Jahani et al.*, 2009]. On one of these profiles, pronounced thinning of Hormuz rocks (and possible welding) is observed next to a buried diapir (Figure 5) *Jahani et al.* [2009]. This particular image also provides a unique glimpse of 1–2 km of older sedimentary rocks underlying the Hormuz Fm. It is not clear whether significant thicknesses of pre-Hormuz strata exist in other parts of the range or whether Hormuz Fm rocks normally lie upon crystalline basement. Here, we use the term "basement" to describe anything underneath the Hormuz Fm, in common with other papers on the Zagros.

Lying above the Hormuz salt is a ~5–10 km thick succession of platform sediments deposited on the northeastern Arabian passive margin during the Paleozoic, Mesozoic, and early Tertiary. The lower and middle cover is only rarely exposed within the SFB itself, but it is thought to comprise Paleozoic and Mesozoic conglomerates, limestones, and dolomites that act as a structurally competent layer, termed the "Competent Group" by *O'Brien* [1957]. Latest Cretaceous and early Tertiary sediments comprise more limestones interbedded with structurally important marl, shale, and evaporite horizons. These are topped by up to ~4 km of additional Miocene-Recent sandstones and conglomerates which mark the diachronous onset of continental collision across the SFB [*Hessami et al.*, 2001; *Fakhari et al.*, 2008; *Khadivi et al.*, 2010]. *O'Brien* [1957] collectively labeled the late Cretaceous and Cenozoic strata the "Upper Mobile Group;" adding this to the underlying Competent Group brings the total Phanerozoic stratigraphic thickness to ~10–15 km [*James and Wynd*, 1965; *Molinaro et al.*, 2004; *Sherkati et al.*, 2005; *Carruba et al.*, 2006; *Casciello et al.*, 2009; *Vergès et al.*, 2011].

Several balanced cross sections across the SFB—incorporating both structural thickening and erosion—provide the main constraints on the depth to basement. Most estimates lie within the range 9–13 km, values which are supported by a series of local microseismicity surveys, each of which shows an increase in body wave velocities below a depth of 10–12 km [*Hatzfeld et al.*, 2003; *Tatar et al.*, 2004; *Nissen et al.*, 2010; *Roustaei et al.*, 2010; *Nissen et al.*, 2011; *Yaminifard et al.*, 2012a, 2012b] (Figure 2a). However, cover thickness estimates in the outer (S and SW) parts of the SFB—especially the Dezful Embayment and coastal Fars Arc

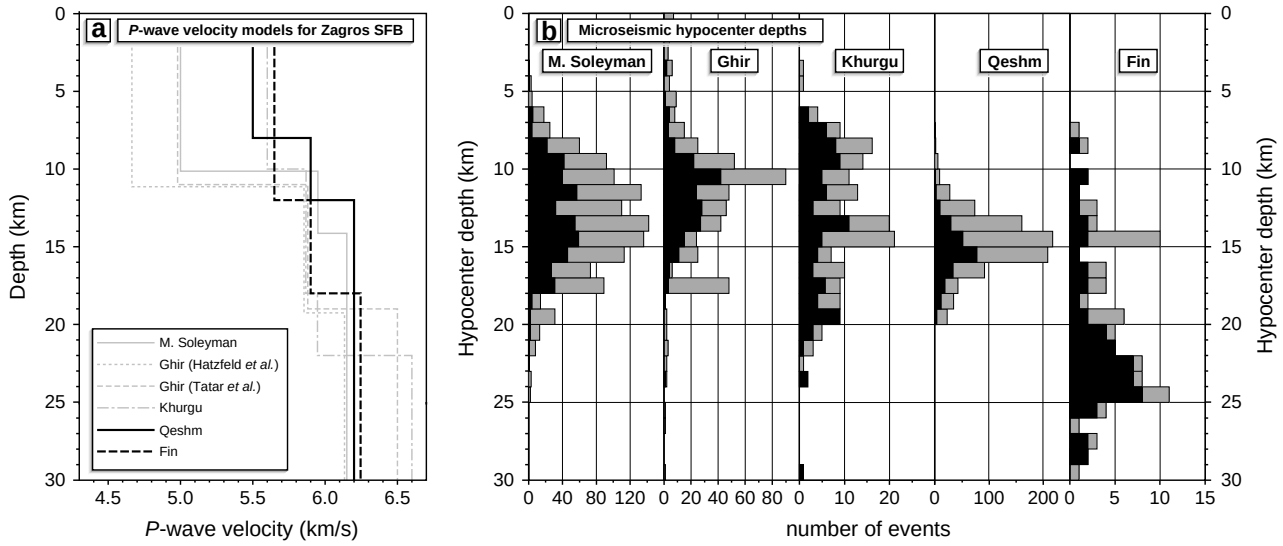

Figure 2. (a) *P* wave velocity models determined from microseismic surveys within the Zagros SFB at Masjed Soleyman [*Nissen et al.*, 2011], Ghir [*Hatzfeld et al.*, 2003; *Tatar et al.*, 2004], Khurgu [*Yaminifard et al.*, 2012b], Qeshm [*Nissen et al.*, 2010], and Fin [*Roustaei et al.*, 2010]. *S* wave velocities were in all cases estimated to be 1.75–1.85 times slower. Because we are interested in seismic velocities within the thick sedimentary cover, we exclude a number of nearby surveys that lie just outside the SFB. Note that velocities within the sedimentary cover at Qeshm and Fin are poorly constrained due to an absence of earthquakes at these depths. (b) Depth distribution of microseismicity obtained from these same surveys. Black bars show the best-resolved earthquake depths, while grey bars represent ones with greater uncertainties (see individual papers for details).

(Figure 1b)—tend to be somewhat greater than those in the inner (N and NE) parts, where exposure levels are deeper [e.g., *Blanc et al.*, 2003; *Sherkati and Letouzey*, 2004; *Jahani et al.*, 2009].

Locally, the best estimates of the cover thickness come from the offshore seismic reflection lines of *Jahani* [2008] and *Jahani et al.* [2009] in the eastern Persian Gulf. Although the exact location of each image is not stated, two of the profiles lie either end of Qeshm Island, our principal focus in this paper. Assuming average *P* wave velocities of 4.7–5.7 km/s (see Figure 2a), the observed ~5–6 s two-way travel times to the Hormuz salt are consistent with a Phanerozoic cover thickness of $\sim 14 \pm 2$ km, values that are somewhat larger than the onshore estimates described previously. This difference is partly due to erosion of the upper part of the cover in the onshore SFB, but it also reflects a genuine thickening of Phanerozoic sediments within the SE coastal Fars Arc [*Jahani et al.*, 2009]. Later, in section 4, we provide limited additional constraints on stratigraphic thicknesses at Qeshm Island using three, previously unpublished, onshore seismic reflection lines. Although these images are not as high quality as the offshore data, derived estimates of the depth to the Hormuz Fm are consistent with those of *Jahani et al.* [2009].

2.2. Structure and Seismicity

Arrays of parallel "whaleback" anticlines and synclines dominate the short-wavelength topography and surface structure of the SFB. These were initially described as detachment folds formed by buckling of the cover along both the Hormuz salt [e.g., *Colman-Sadd*, 1978]. However, more recent structural data show that shallower décollements within the middle sedimentary cover are also important in generating surface folding [e.g., *Sherkati et al.*, 2005; *Carruba et al.*, 2006; *Sepehr et al.*, 2006; *Vergès et al.*, 2011]. Numerical models of the SFB also require multiple décollements in order to reproduce observed fold spacing as well as the predominance of folding over faulting [*Yamato et al.*, 2011]. However, an alternative interpretation (which can also balance observed cross sections of the surface geology) invokes fault propagation folding above steep reverse faults that branch upward into the cover from a detachment in Hormuz salt [*McQuarrie*, 2004]. An additional, complicating factor is the potential role of Hormuz diapirism in localizing this folding and faulting, particularly in the eastern Fars Arc where salt plugs are most prevalent [*Jahani et al.*, 2009]. Unfortunately, there is a scarcity of published, onshore seismic reflection data against which these competing models could be tested directly.

Although strike-slip faulting plays an important role in the central SFB, most earthquakes in the range involve steeply dipping, blind reverse faults, their 30–60° dips possibly inherited from normal faults in the stretched Arabian continental margin [e.g., *Jackson*, 1980; *Berberian*, 1995; *Talebian and Jackson*, 2004]

(Figure 1b). Another notable characteristic of the SFB is the predominance of moderate-sized earthquakes (M_w 5–6) and the complete absence of any larger than M_w ~7 in instrumental catalogs [*Nissen et al.*, 2011]. This also appears to be true of the ~1000 year historical record [*Ambraseys and Melville*, 1982]. Summed earthquake moment tensors can account for less that 10% of the convergence rate measured with GPS or plate motion models [*Jackson and McKenzie*, 1988; *Masson et al.*, 2005]. Epicenters are spread across a 100–200 km wide zone in the southern and southwestern SFB, approximately colocated with the locus of GPS shortening, and almost all are situated below the regional, smoothed ~1250 m contour [*Nissen et al.*, 2011]. This supports the idea that the range has propagated toward its foreland over time [e.g., *Hessami et al.*, 2001; *Mouthereau*, 2011], possibly promoted by stresses introduced by sediment ponding within internally draining basins that have developed in certain parts of the interior SFB [*Walker et al.*, 2011]. However, the cutoff in seismicity (~1250 m) is at a noticeably lower smoothed elevation than the High Zagros and Central Iranian plateau, which are at 1500–2500 m [*Nissen et al.*, 2011] and *Allen et al.* [2013]. This hints that aseismic processes are responsible for the additional crustal thickening required to raise the northeastern SFB, the High Zagros, and the adjacent Central Iranian plateau to their current regional elevations.

Accurately characterizing the depth and orientation of these faults could potentially help distinguish between competing structural and mechanical models of the Zagros. However, there is controversy over whether earthquake faulting occurs mainly within the sedimentary cover, the underlying basement, or a mixture of the two. The scarcity of mapped surface faults and the total absence of *coseismic*, primary surface rupturing in the SFB have resulted in a widely held assumption that earthquakes are strongly concentrated within the basement. The presence of a discrete number of major basement faults is supported by sudden changes in stratigraphic level (up to a few kilometers) across certain anticlines [*Berberian*, 1995]. This view is also consistent with local microseismic surveys which all show a concentration of events at basement depths [*Hatzfeld et al.*, 2003; *Tatar et al.*, 2004; *Nissen et al.*, 2010; *Roustaei et al.*, 2010; *Nissen et al.*, 2011; *Yaminifard et al.*, 2012a, 2012b]. In the eastern Fars Arc, cross-cutting relations suggest that these basement faults developed relatively late on (in the Pliocene) following an earlier thin-skinned phase of deformation [*Molinaro et al.*, 2005; *Sherkati et al.*, 2005].

However, centroid depths of larger SFB earthquakes derived from modeling teleseismic body waveforms [*Jackson and Fitch*, 1981; *Kadinsky-Cade and Barazangi*, 1982; *Jackson and McKenzie*, 1984; *Ni and Barazangi*, 1986; *Baker et al.*, 1993; *Priestley et al.*, 1994; *Maggi et al.*, 2000; *Talebian and Jackson*, 2004; *Adams et al.*, 2009; *Nissen et al.*, 2011] (Figure 1b) are more consistent with rupture of the "Competent Group" of sediments making up the lower and middle parts of the cover [*Nissen et al.*, 2011]. Roughly three quarters of the 80 centroid depths determined in this way lie within the range 4–10 km, consistent with this scenario (Figure 1c). These figures exclude earthquakes occurring in the High Zagros—principally along the Main Recent Fault—and a distinct set of deeper, shallow-angle thrust events in the northern part of the Oman Line (Figure 1b). For a discussion of these events, which all lie outside the SFB, see *Talebian and Jackson* [2004].

The two earthquake sequences which are the focus of this paper commenced with initial M_w ~6 reverse faulting events at Qeshm Island on 27 November 2005 and at Fin on 25 March 2006, both in the southeastern part of the SFB (Figure 1b). These main shocks were the first earthquakes of this magnitude in the Zagros for which InSAR data were available, thereby offering fresh opportunities to investigate the depth extents of faulting and its relationship with surface structures.

3. Previous Work on the Qeshm and Fin Earthquake Sequences

3.1. Qeshm Main Shock Event

The initial event in this sequence was a M_w ~6.0 reverse faulting earthquake that struck central Qeshm Island at 10:22 UTC on 27 November 2005 (Figure 3a). Qeshm Island had previously experienced a number of large historical earthquakes, including destructive events in 1884, 1897, and 1902 which collectively killed around 1000 people [*Berberian and Tchalenko*, 1976]. The 2005 main shock badly damaged several villages, killing 13 people and injuring a further ~100. Small cracks observed along the axis of a NNE-trending syncline were probably caused by minor bedding plane slip, and there were no primary surface ruptures [*Nissen et al.*, 2007b].

Three coseismic interferograms—one ascending and two descending—were available from Envisat Advanced Synthetic Aperture Radar (ASAR) data, each using independent preearthquake and postearthquake scenes (Figures 3b–3d). Modeling these interferograms, *Nissen et al.* [2007b] suggested that

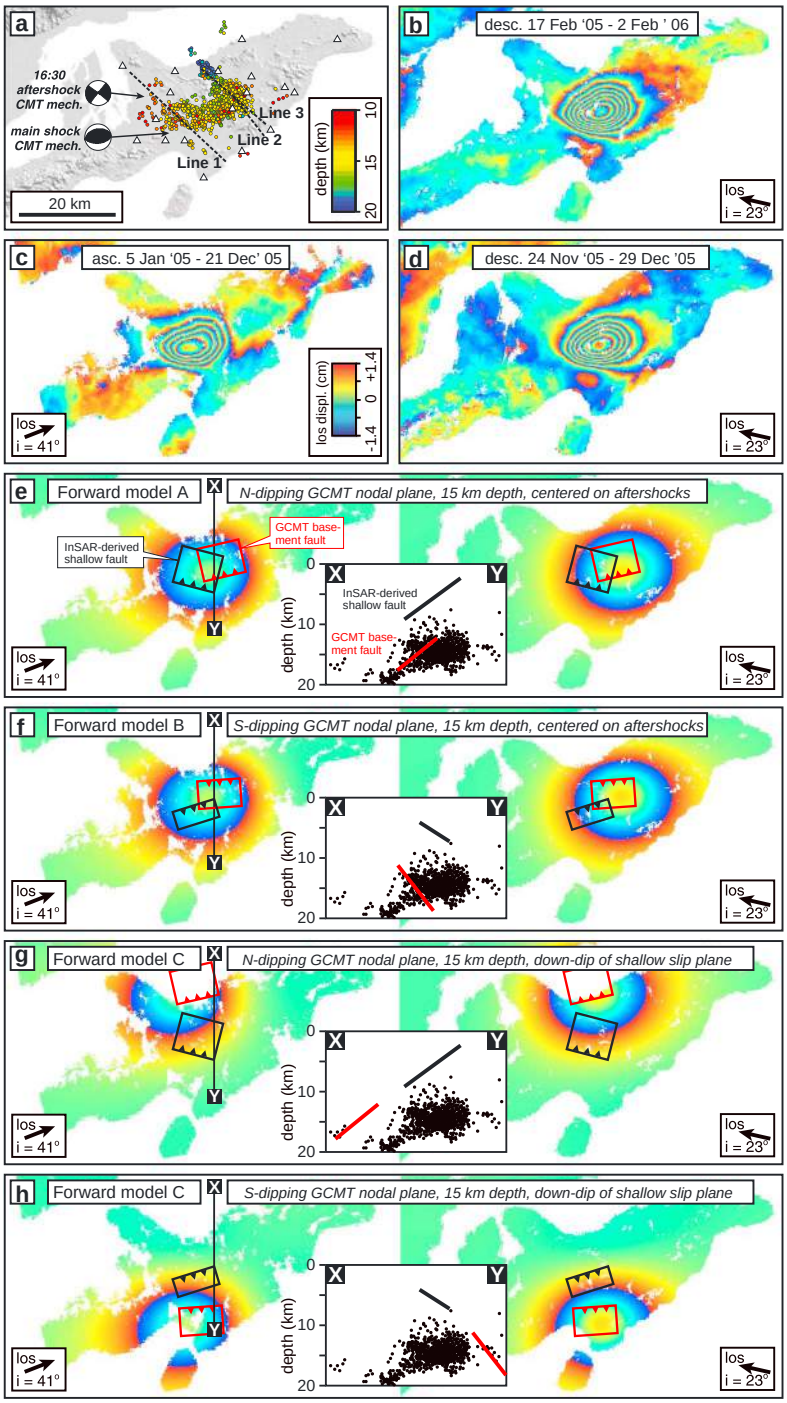

Figure 3. (a) GCMT mechanisms of the M_w 6.0 main shock and M_w 5.5 aftershock of 27 November 2005, with arrows pointing toward their USGS (NEIC) preliminary determination of epicenters. Circles show smaller aftershocks, colored according to hypocenter depth, recorded at the local stations marked by triangles. Dashed black lines mark the seismic reflection lines in Figure 4. (b–d) Interferograms spanning the main shock (see *Nissen et al.* [2010] for details). An ascending interferogram is shown in Figure 3, and the two independent descending-track interferograms are shown in Figures 3b and 3d. (e–g) Model interferograms for the GCMT main shock mechanism centered at a depth of 15 km, with areas that are incoherent in the real interferograms masked out. The map extents of the GCMT basement fault used to synthesize the interferogram are shown by the red rectangle. In each case, the left-hand side shows the ascending interferogram and the right-hand side shows the descending-track interferogram. Map extents of the shallow model faults of *Nissen et al.* [2010]—derived from modeling of the interferograms in Figures 3b–3d—are marked by black rectangles. The inset panels show cross sections along the line *X*-*Y* through the microseismic aftershocks (black dots) and the model faults (black and red lines for shallow InSAR-derived slip plane and basement GCMT plane, respectively).

the earthquake ruptured a blind, north (N)-dipping reverse fault with slip centered ~6 km below the surface. Their uniform slip model fault spanned the depth range 3–9 km, although the top and bottom depths are less well constrained than the fault center depth due to a strong trade-off between fault width and slip magnitude. Subsequent reevaluations of these same data by *Nissen et al.* [2010] and *Lohman and Barnhart* [2010] highlighted the possibility that the earthquake ruptured a SSE-dipping fault, with slip concentrated at similar depths as for the N-dipping model fault. Fault width-lip magnitude trade-offs and dip direction ambiguities are common features of geodetic models of earthquakes that are buried to depths of a few kilometers [*Massonnet and Feigl*, 1995; *Lohman et al.*, 2002; *Roustaei et al.*, 2010; *Elliott et al.*, 2011].

The earthquake was also well recorded by stations of the Global Digital Seismographic Network (GDSN). Body waveform modeling by *Nissen et al.* [2007b, 2010] yielded a centroid depth of ~9 km, slightly deeper than one would expect from the InSAR-derived fault model but within the margin of error of ±3–4 km commonly quoted for such models. In addition, the Qeshm main shock was chosen by *Fox et al.* [2012] as a test event for their method of determining earthquake source parameters depths from intermediate-period surface wave amplitude spectra. Their resulting centroid depth of ~7 km is in close agreement with the body waveform solution and with the InSAR-derived fault models.

Of the other seismological source parameters, the moment shows the most notable discrepancy with the InSAR-based models. The InSAR-derived moment is roughly double that of the minimum-misfit body waveform moment, ~60% larger than the USGS National Earthquake Information Center (NEIC) moment and ~20% larger than the Global Centroid Moment Tensor (GCMT) and *Fox et al.* [2012] moment. However, discrepancies of up to 0.2 M_w units between InSAR-derived and seismologically derived moments are not uncommon [e.g., *Weston et al.*, 2012]. In this case, the larger InSAR moment probably reflects the contribution of small amounts of aseismic deformation, possibly including some afterslip at the shallow end of the seismic fault plane which could also help account for the small differences in model depths [*Nissen et al.*, 2010].

3.2. Qeshm Aftershocks

The initial earthquake was followed by intense aftershock activity spanning almost four years, including a second M_w ~6 event in 2008 in close proximity to the 2005 main shock [*Nissen et al.*, 2010; *Lohman and Barnhart*, 2010]. However, the focus of this paper is only the first four months of aftershock activity.

No local seismometers were in place at the time of the main shock, but a few early aftershocks were widely recorded by GDSN stations. The largest of these was a M_w ~5.5 strike-slip earthquake with a centroid depth of ~10 km that occurred at 16:30 UTC, roughly 6 h after the initial event and a few kilometers to the NW (Figure 3a) *Nissen et al.* [2010]. Starting a week after the initial earthquake, a network of eighteen portable seismometers was installed across central and eastern Qeshm Island [*Nissen et al.*, 2010; *Yaminifard et al.*, 2012a] (Figure 3a). Around 2000 earthquakes were detected between 6 December 2005 and 26 February 2006, when the network was disbanded, ranging in magnitude from ~1 to 3.7. *P* and *S* arrival times were inverted to jointly determine the earthquake hypocenters and a 1-D velocity structure, and first motion polarities were used to estimate focal mechanisms for the best-recorded events. None of these aftershocks were well recorded teleseismically, so we cannot directly compare the mechanisms and depths obtained from local arrival times with any obtained from body waveform modeling.

Preliminary results were published by *Nissen et al.* [2010] with additional hypocenters later provided by *Yaminifard et al.* [2012a]. Both studies show a cluster of aftershocks centered beneath the eastern part of the InSAR deformation signal (Figure 3a). These are concentrated at depths of 14–16 km—well below the slip range determined from InSAR modeling—and there is a rapid drop-off in the number of earthquakes at shallower depths, with only a small number of events reliably located within the cover (Figure 2b). By modeling the first motion polarities of some of the best-recorded events, *Yaminifard et al.* [2012a] suggested that they were predominantly strike slip, mostly with NW-, North- or NE-trending *P* axes.

The initial interpretation of these results suggested that the main shock ruptured the "Competent Group" of limestones and dolomites within the midlower sedimentary cover and that this triggered basement microseismicity beneath the Hormuz Fm [*Nissen et al.*, 2010]. However, the triggering mechanism was unclear; although some of aftershocks occurred in areas exhibiting positive Coulomb stress changes imparted by the main shock (up to 0.05 MPa), a few occurred in areas with negative stress changes [*Nissen et al.*, 2011]. An

obvious limitation of these Coulomb models is their assumption of an elastic half-space, despite the known presence of weak Hormuz salt.

3.3. Fin Main Shock and Initial Aftershocks

The first and largest earthquake in this sequence occurred near the town of Fin, ~50 km north of Qeshm Island, at 07:29 UTC on 25 March 2006. It involved E–W-oriented reverse faulting with a moment magnitude in the range 5.7–5.9 and was soon followed by aftershocks of M_w 5.5, 5.2, 5.0, and 4.9, all occurring on the same day and all with similar mechanisms. Calibrated relocations of these five earthquakes indicate that they occurred along strike from one another, spanning a total distance of ~15 km [*Roustaei et al.*, 2010]. Modeling three descending-track and one ascending-track coseismic interferograms, *Roustaei et al.* [2010] found that the dip direction of the fault could not be positively identified, much like at Qeshm. However, the top and bottom of the rupture were both well resolved, at 5–6 km and 9–10 km, respectively. These figures are in good agreement with the same authors' body waveform model, whose centroid depth is ~8 km. Body waveforms of the largest aftershock (09:55 UTC) were also modeled, yielding a centroid depth of ~4 km.

3.4. Fin Microseismic Aftershocks

As at Qeshm, portable seismometers were soon deployed to collect additional aftershock data. Four seismometers were installed in the epicentral area in mid-April and operated until mid-May 2006 [*Roustaei et al.*, 2010]; these were complemented by a further 18 in the Tiab region to the northeast where another large earthquake had just struck [*Gholamzadeh et al.*, 2009]. A diffuse array of ~400 aftershocks, ranging in magnitude between 1 and 4, were recorded in the Fin region. Hypocenter depths are concentrated within the basement with a small peak in aftershock numbers at ~14–15 km and a larger one at ~20–25 km (Figure 2b). Due to the small number of seismometers deployed in the epicentral area, robust first motions mechanisms could not be obtained as they had at Qeshm.

3.5. "Phantom Earthquake" Reinterpretation

More recently, *Barnhart and Lohman* [2013] completely reinterpreted the sequence of events at Qeshm and Fin, based on an assumption that the initial main shock events occurred at the same (basement) depths as the microseismic aftershocks. This implies that the InSAR-derived fault slip—which is undoubtedly shallow—occurred aseismically, in what the authors term phantom earthquakes. These aseismic slip events are inferred to have occurred on fault zones which are permeated with Hormuz salt and which lie directly updip from the seismogenic fault planes in the basement. This is an intriguing proposition, because if large pulses of aseismic slip were a common occurrence following earthquakes in the SFB, then they could help account for the large (approximately 10:1) discrepancy between GPS and seismic shortening rates [*Jackson and McKenzie*, 1988; *Masson et al.*, 2005], a possibility which was further explored by *Barnhart et al.* [2013].

However, there are some obvious potential problems with this reinterpretation of events. First, there are conspicuous coincidences in the mechanisms, magnitudes, and geographic locations of the aseismic slip events with those of the preceding earthquakes. Second, *Barnhart and Lohman* [2013] and *Barnhart et al.* [2013] stated that uncertainties in the Qeshm and Fin body waveform model centroid depths are large enough to permit main shock slip at the level of the aftershocks but did not test this assumption with any waveform modeling of their own.

The phantom earthquake interpretation therefore depends upon the following two premises. (1) The geodetic data must permit a M_w 6 reverse-faulting earthquake centered at basement depths and in close proximity to the microseismicity. Surface deformation caused by this earthquake must be masked within the interferograms by a combination of the larger signal from shallow aseismic slip, atmospheric noise, and (in the Qeshm case) by partly lying offshore. We investigate this point in section 5.2. (2) Forcing the body wave model from its preferred centroid depth to basement depths should not lead to any clear deterioration in the misfit between observed and synthetic waveforms. This requires that depth errors in the original minimum-misfit solutions are slightly larger (at ~6–7 km) than those commonly quoted in studies of this kind (~3–4 km). We test this assertion in section 6.

4. Seismic Reflection Profiles of Qeshm Island

In this short section, we provide further constraints on the subsurface structure and stratigraphy of Qeshm Island using previously unpublished National Iranian Oil Company (NIOC) seismic reflection data in close proximity to the Qeshm earthquakes (Figure 4). The three NW–SE-trending seismic reflection lines are

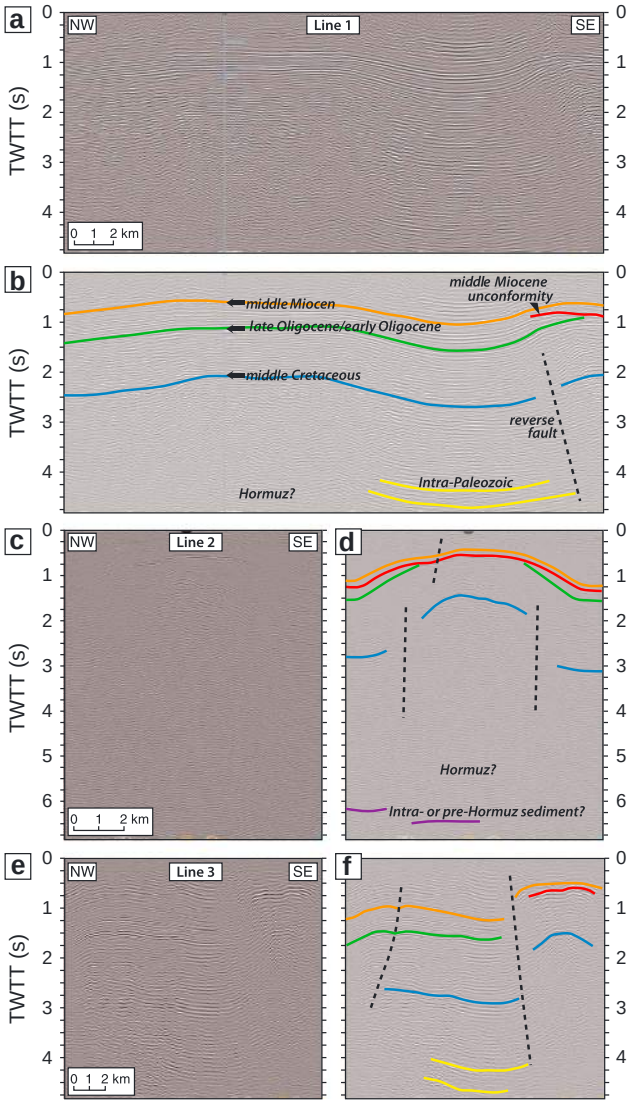

Figure 4. Three NW-SE seismic reflection lines across central Qeshm Island (see Figure 3a for locations). TWTT is the two-way travel time in seconds. (a and b) Uninterpreted and interpreted views of line 1; direct constraints on the depth to the Cenozoic reflectors are provided by nearby wells. (c and d) Uninterpreted and interpreted views of line 2. (e and f) Uninterpreted and interpreted views of line 3, with reflectors colored as in Figure 4a.

plotted on Figure 3a; line 1 (Figures 4a and 4b) probably lies close to the western end of the Qeshm main shock faulting, while lines 2 (Figures 4c and 4d) and 3 (Figures 4e and 4f) are a few kilometer to its east. Direct constraints on the depths to Cenozoic and Mesozoic reflectors are provided by nearby wells; for further interpretation, we follow the approach of *Jahani* [2008] and *Jahani et al.* [2009].

Although these profiles are not as high quality as some of those presented by *Jahani et al.* [2009], they nevertheless provide useful constraints on the depth to the Hormuz Fm. In lines 1 and 3 (Figures 4a–4b and 4e–4f), the deepest clear reflectors are intra-Paleozoic sediments at 4–4.75 s two-way travel time (TWTT); these are at the same level as similar intra-Paleozoic reflectors in *Jahani et al.* [2009, Figure 5], an image in which the underlying Hormuz salt can also be observed. In line 2, we interpret deeper reflectors at 6–6.5 s TWTT as intra- or sub-Hormuz sediments (Figures 4c and 4d). Again, these reflectors lie at the same TWTT as similar features in *Jahani et al.* [2009, Figure 5]. Collectively, these observations give us confidence that the Phanerozoic (post-Hormuz) cover thickness at Qeshm Island is very similar to the estimate of $\sim 14 \pm 2$ km derived from the offshore reflection lines of *Jahani et al.* [2009] using average *P* wave velocities of 4.7–5.7 km/s (Figure 2a).

Although there are clear indications of faulting within the middle part of the sedimentary cover—especially in line 3 (Figures 4e and 4f)—faulting in the location expected from the dislocation models of *Nissen et al.* [2010] and *Lohman and Barnhart* [2010] is difficult to observe. This may be because the reflection lines lie at the western end (line 1) and a few kilometers east (lines 2 and 3) of the faulting (Figure 3).

5. InSAR Modeling at Qeshm

5.1. Robustness of InSAR-Constrained Fault Depths

We begin this section by testing the robustness of the InSAR-constrained fault depth estimates [*Nissen et al.*, 2007b, 2010; *Lohman and Barnhart*, 2010], using new elastic dislocation models that incorporate a plausible range of elastic moduli [*Okada*, 1985]. We focus on the Qeshm earthquake, which is larger than the Fin main shock and has both a clearer InSAR signal and a better-constrained aftershock distribution.

The Qeshm fault model of *Nissen et al.* [2010] assumed an elastic half-space with Lamé parameters $\mu = \lambda = 2.9 \times 10^{10}$ Pa and a Poisson ratio $\nu = 0.25$, values which are consistent with the cover seismic velocities derived by analyzing locally recorded aftershocks. *Lohman and Barnhart* [2010] and *Barnhart and Lohman* [2013] also used a half-space but did not state its elastic moduli. In this reanalysis, we use a range of μ, λ, and ν values, but our model setup is otherwise identical to that of *Nissen et al.* [2010] (including the fixing of slip magnitude, for the reasons explained in section 3.1). Varying μ and λ but keeping $\nu = 0.25$ strongly influences the seismic moment but does not alter the slip depth range. Varying ν between 0.05 and 0.4—a spread of values that characterizes all common igneous and sedimentary rock types, including rock salt [e.g., *Gercek*, 2007]—alters the top and bottom fault depths by <0.5 km and the fault center depth by <0.25 km.

We should also consider the possible impact of rheological layering on the observed surface deformation and thus the depth range of model fault slip [e.g., *Chinnery and Jovanovich*, 1972; *Savage*, 1987]. Depth-dependent elasticity most strongly influences surface displacements generated by faulting with substantial horizontal slip components [*Pollitz*, 1996], and strike-slip earthquakes can consequently appear significantly deeper in layered models than in homogeneous half-spaces [e.g., *Hearn and Bürgmann*, 2005; *Dubois et al.*, 2008]. For moderate-magnitude, dip-slip earthquakes which have been modeled in both homogeneous and layered elasticities, significant local discrepancies in fault slip are also possible but overall top and bottom fault depths differ by less than 10% [*Lohman et al.*, 2002; *Trasatti et al.*, 2011; *Bie et al.*, 2014]. This is probably also true for the Qeshm main shock, particularly as horizontal motions for this earthquake are mostly oriented N-S and therefore not well recorded by InSAR.

Fault depth errors arising from uncertainties in elastic structure are therefore probably small compared to the observed separation of main shock and aftershocks. This confirms that the faulting responsible for the large InSAR signal observed on Qeshm Island—whether it be seismic or aseismic—lies within the sedimentary cover rather than in the underlying basement.

5.2. A Hidden Main Shock Earthquake in the Basement?

Next, we explore *Barnhart and Lohman*'s 2013 assertion that a M_w 6 reverse faulting earthquake could be colocated with the microseismic aftershocks and be invisible to InSAR. To do this, we generated a new series of elastic dislocation models and synthetic interferograms for a M_w 6 basement source event and compared these to the observed interferograms and microseismicity (Figures 3a–3d). For our basement main shock earthquake, we tried both nodal planes of the GCMT focal mechanism—strikes, dips, and rakes of 257°/39°/83° and 86°/51°/96°—and centered the source at a depth of 15 km within an elastic half-space with Lamé parameters $\lambda = \mu = 3.0 \times 10^{10}$ Nm. By assuming uniform slip of 0.44 m on a square fault plane with dimensions of 8.8 km, our model earthquakes reproduce the observed GCMT moment of 1.03×10^{18} Nm and have realistic slip-to-length ratios of 5×10^{-5} [*Scholz*, 1990].

In model A, we centered the N-dipping GCMT fault plane in the middle of the aftershock cluster at 26° 51′ N, 55° 58′ E (Figure 3e). In model B, we did the same using the south (S)-dipping GCMT nodal plane (Figure 3f). Ascending and descending forward model interferograms contain 1 and 1.5 fringes, respectively, located in approximately the same place as the outermost fringes of the observed deformation signals (Figures 3b–3d). In both N- and S-dipping cases, the basement model faults lie within the aftershock cloud, almost directly beneath the InSAR-derived faults in the midlower sedimentary cover. Basing the model fault plane parameters on the body waveform mechanism of *Nissen et al.* [2010], as opposed to the GCMT solution, does not significantly alter these results.

These models confirm that shallow aseismic slip could, potentially, mask a basement main shock colocated with the microseismicity, as was suggested by *Barnhart and Lohman* [2013]. However, the aseismic fault slip in the cover occurs directly above the basement faulting rather than updip from it, which is where Coulomb stress changes that might drive a phantom earthquake are likely to be greatest.

Next, we generated two more forward models in which the basement main shock earthquake was situated directly downdip from the shallow aseismic slip planes, a configuration which makes more sense in terms of Coulomb stress transfer. In model C we used the N-dipping GCMT nodal plane (Figure 3f) and in model D we used the S-dipping one (Figure 3g).

In both cases, roughly half of the surface deformation signal now lies offshore. However, the onshore part lies outside the main observed fringe pattern in what are relatively "flat" parts of the real interferograms. This onshore deformation is similar in magnitude to the short-wavelength phase changes—most likely from atmospheric noise—observed in distal parts of Qeshm Island. It would be remarkably coincidental for this deformation signal to be masked in all three interferograms, each constructed from independent radar acquisitions. A further issue with this configuration is that the basement faulting now lies well outside the main aftershock cluster, in areas where very few aftershocks were detected despite good station coverage. Again, using the body waveform model nodal planes of *Nissen et al.* [2010], rather than those of the GCMT solution, makes no significant difference to these results.

In summary, the inference of a ~15 km-deep, M_w 6 reverse faulting earthquake at Qeshm Island simply replaces one apparent paradox—the puzzling vertical separation of main shock and aftershocks [*Nissen et al.*, 2010]—with other, equally perplexing ones. On the one hand, for such an earthquake to be masked in the interferograms by shallow aseismic slip, it would need to have occurred directly beneath the aseismic slip fault (not down dip from it). Although spatial relations of this kind are not unprecedented—some aftershocks of the 1999 Chi-Chi earthquake occurred directly underneath the subparallel main shock fault at a vertical distance of ~15 km [*Kao and Chen*, 2000]—the Qeshm case does require a remarkable coincidence in geographical position to go along with the ones in mechanism and moment. On the other hand, if it occurred downdip of the shallow slip plane—as suggested by *Barnhart and Lohman* [2013]—then it would be horizontally offset from the aftershock cloud by a few kilometers. In this instance, its surface deformation would also probably be visible in at least one of the three, entirely independent, coseismic interferograms.

6. Body Waveform Modeling

The purpose of this section is to better constrain the centroid depths of the main shocks and largest initial aftershocks at Qeshm (10:22 and 16:30 UTC, 27 November 2005) and Fin (07:29 and 09:55 UTC, 25 March 2006) using teleseismic body waveform modeling. By accounting for the separation between direct arrivals *P* and *S* and near-source surface reflections *pP*, *sP*, and *sS*, this is the best available way of determining the depth at which main shock *seismic* slip was centered [e.g., *Molnar and Lyon-Caen*, 1989]. By using body waveforms whose wavelengths are longer than the causative faulting, the earthquake appears as a point source in space (the "centroid") whose depth represents the collapsed average of the seismic slip distribution. Furthermore, the resulting source models are insensitive to short-wavelength variabilities in fault slip and local velocity structure. Although there is no established way of obtaining formal errors in centroid depth (or any other parameter), uncertainties of 3–4 km are quoted in many body waveform modeling studies [e.g., *Fredrich et al.*, 1988; *Molnar and Lyon-Caen*, 1989; *Taymaz et al.*, 1990; *Maggi et al.*, 2000; *Talebian and Jackson*, 2004; *Emmerson et al.*, 2006]. These are a considerable improvement on the 10–15 km errors typical of the EHB catalog, currently the most accurate, automated register of earthquake depths [*Engdahl et al.*, 1998, 2006].

As described in section 3, minimum-misfit source parameters for these earthquakes have already been published by *Nissen et al.* [2007b], *Nissen et al.* [2010], and *Roustaei et al.* [2010]. *Barnhart and Lohman* [2013] suggested that uncertainties in these centroid depths are large enough to permit main shock slip at the same (basement) depths as the aftershocks, but they did not actually test this assumption using body waveform modeling. In this section, we investigate how tightly constrained the centroid depths are, especially considering realistic uncertainties in the seismic velocity structure above the earthquake source.

As in the previous studies, we used broadband GDSN seismograms downloaded from the Incorporated Research Institutions for Seismology (IRIS) Data Management Center and deconvolved so as to mimic the

response of World-Wide Standardized Seismograph Network 15–100 s long-period instruments. Vertical component seismograms were used to model *P*, *pP*, and *sP* phases, and transverse component seismograms were used for the *S* and *sS* phases. Stations were restricted to the distance range 30°–90° (for *P* waves) and 30°–80° (for *SH* waves) in order to avoid complications from the Earth's crust and core. For three out of four earthquakes modeled here, we find a good azimuthal spread of stations except for the southeastern quadrant of the focal sphere, roughly corresponding to the Indian Ocean. However, for the Qeshm 16:30 UTC aftershock, many of these seismograms were too noisy to be used in the modeling and we had to make do with a more restricted station coverage [see *Nissen et al.*, 2007b, Figure 10].

We used the MT5 version [*Zwick et al.*, 1994] of the weighted least-squares algorithm of *McCaffrey and Abers* [1988] and *McCaffrey et al.* [1991] to jointly invert the *P* and *SH* waveforms for the best-fit strike, dip, rake, scalar moment, centroid depth, and source time function, the latter comprising a series of overlapping isosceles triangles, each having a half-duration of 1 s. The routine minimizes the weighted squared residuals between observed waveforms and synthetic seismograms computed by combining direct arrivals (*P* or *S*) with near-source reflections (*pP* and *sP*, or *sS*). Synthetic waveform amplitudes were corrected for geometrical spreading [*Langston and Helmberger*, 1975] and for anelastic attenuation using a Futterman *Q* operator with a t^* of 1.0 s for *P* and 4.0 s for *SH* waves [*Futterman*, 1962]. Uncertainties in t^* result in uncertainties in source duration and moment but have little effect on other source parameters [*Fredrich et al.*, 1988; *Maggi et al.*, 2000]. Before inverting the data, onset times were checked against high-frequency broadband records, thus mitigating against any potential biases due to epicentral mislocation. The seismograms were also weighted according to azimuthal density, with weights of *SH* waveforms further halved to compensate for their generally larger amplitudes.

6.1. Qeshm Earthquakes

6.1.1. Main Shock

We start by investigating the centroid depth of the Qeshm main shock. Initially, we assumed the same seismic velocity structure as *Nissen et al.* [2010] (Figure 5a), a slight simplification of the one obtained through inverting local aftershock arrival time data. We fixed the centroid depth to a series of values at 1 km intervals either side of the minimum-misfit value (9 km) and solved for the minimum-misfit strike, dip, rake, moment, and source time function at each depth. For each model run, we also recorded the normalized error, defined as the percentage ratio of the weighted residual variance to the weighted data variance ("R/D %").

Resulting model focal mechanisms are plotted according to their normalized error (*x* axis) and centroid depth (*y* axis) in Figure 5a, while visual comparisons of observed and synthetic seismograms are shown for four of these models—with centroid depths 6 km, 9 km, 12 km, and 15 km—in Figure 6a. Within the centroid depth range 6–10 km, normalized errors change little, with values <10% greater than for the minimum-misfit solution. Correspondingly, there is little visual change in the fit between observed and synthetic waveforms (Figure 6a, first two lines).

However, as the centroid depth is forced further away from the minimum-misfit solution, the normalized errors increase more rapidly. At a centroid depth of 12 km, there is a clear degradation in the fit between observed and synthetic waveforms (Figure 6a, third line). On both *P* and *SH* seismograms, synthetic pulses are now noticeably longer than observed ones; in the *SH* case, synthetic wavelet amplitudes are also too small. At a centroid depth of 15 km—the approximate value cited in the "phantom earthquake" interpretation of the Qeshm sequence [*Barnhart and Lohman*, 2013]—the normalized error is more than twice that of the minimum-misfit solution and the match between observed and synthetic waveforms deteriorates further (Figure 6a, fourth line).

The modeling results also exhibit a clear, inverse trade-off between centroid depth and scalar moment. At a centroid depth of 15 km, the moment is 50–100% smaller than independent estimates from the USGS NEIC and GCMT catalogs and from *Fox et al.* [2012] (Figure 5b). The moment is the least well constrained of the body waveform source parameters, due to its strong reliance on the assumed density (we used 2700 kg/m^3 above 12 km and 2800 kg/m^3 below 12 km) as well as uncertainties in the attenuation of body wave amplitudes. In addition, body waveform models often have slightly lower moments than those of the GCMT catalog, whose inversion of longer wavelengths might be expected to capture the source more completely [e.g., *Molnar and Lyon-Caen*, 1989; *Nissen et al.*, 2007a; *Elliott et al.*, 2010]. Nevertheless, the moment discrepancy for the Qeshm main shock is slightly larger than normal for these type of analyses. If, on the other hand, the body wave centroid depth is *raised* from its minimum-misfit value of 9 km, the moment

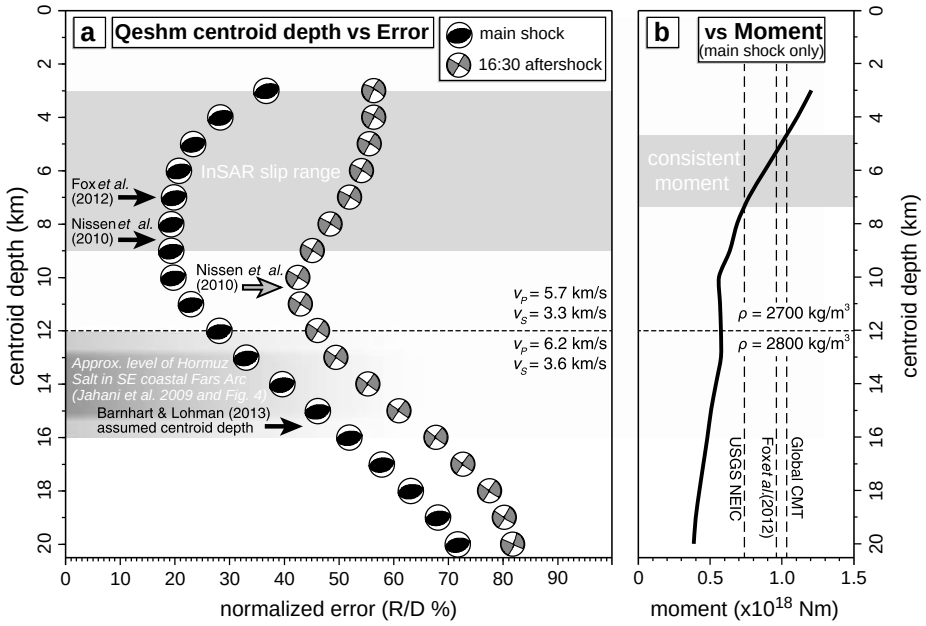

Figure 5. (a) Body waveform models of the 27 November 2005 Qeshm main shock (black) and its largest initial aftershock (grey), plotted as a function of their (fixed) centroid depths and normalized errors (these are a measure of goodness of fit between model and observed *P* and *SH* waveforms). We used the same velocity structure as *Nissen et al.* [2010], shown on the right. Minimum-misfit centroid depths for the main shock, from *Nissen et al.* [2010] and *Fox et al.* [2012], together with the assumed depth of *Barnhart and Lohman* [2013], are picked out by black arrows. The minimum-misfit centroid depth of the aftershock is marked by a grey arrow. The grey area shows the slip extents derived from InSAR [*Nissen et al.*, 2010] and the estimated depth of the Hormuz salt in the SE coastal Fars Arc [*Jahani et al.*, 2009]. (b) The black line shows the body waveform model moment of the main shock as a function of centroid depth. The assumed density structure (that used by *Nissen et al.* [2010]) is shown on the right-hand side. Vertical lines show independent estimates of the moment from the GCMT catalog, the USGS National Earthquake Information Center (NEIC), and *Fox et al.* [2012]. The grey area highlights the depth range of body waveform models whose moment is consistent with these independent estimates.

discrepancy soon vanishes. At centroid depths of 5–7 km, the body wave moment is consistent with the range of estimates provided by the NEIC, GCMT, and *Fox et al.* [2012] solutions (Figure 5b).

In our view, the body wave model with a centroid depth of ~6 km best accounts for these various observations. First, this depth agrees closely with the InSAR-derived slip range and with *Fox et al.*'s [2012] surface wave model (Figure 5a). Second, the corresponding moment lies at the center of the range provided by independent seismological estimates (Figure 5b). Last, the normalized error is only ~7% larger than that of the minimum-misfit solution, and there is no visual deterioration in the match between observed and synthetic waveforms (Figure 6a, first two lines).

6.1.2. 16:30 UTC Aftershock

Next, we repeated the experiment for the 16:30 UTC strike-slip aftershock. Model focal mechanisms are shown in grey in Figure 5a, plotted according to their centroid depth and normalized error. Although normalized errors are higher than for the main shock (due partly to a lower signal-to-noise ratio), there is still a well-defined minimum corresponding to a centroid depth in the lowermost sedimentary cover. It is highly unlikely to have been centered at the ~15 km depth of the peak in microseismic activity, the normalized errors for this model being 50% larger than for the minimum-misfit solution.

6.1.3. Consideration of Seismic Velocities

So far, we have used the same *P* and *S* wave velocities as *Nissen et al.* [2010] (shown in Figure 5a), which were based on the local 1-D velocity structure determined during their inversion of microseismic data. However, there may be significant uncertainties in these velocities, especially within the sedimentary cover where there was a near-total absence of microseismic events. Uncertainties in seismic velocities above the earthquake source control the *P-pP*, *P-sP*, and *S-sS* travel delays and will thus influence the minimum-misfit centroid depths obtained from body waveform analysis. (In the same way, uncertainties in seismic velocities *below* the earthquake source will have no effect on these results).

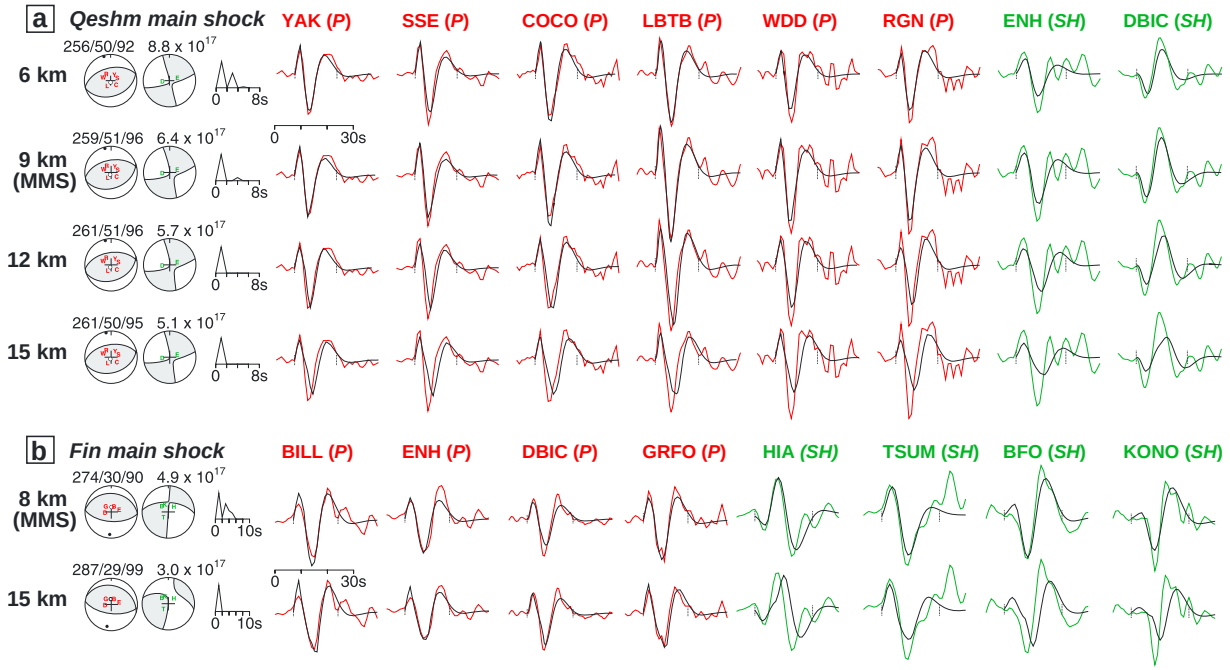

Figure 6. Depth sensitivity tests for (a) the 27 November 2005 Qeshm main shock and (b) the 25 March 2005 Fin main shock, using the same seismic velocity structures as *Nissen et al.* [2010] and *Roustaei et al.* [2010], respectively. Eight representative stations were chosen to illustrate the influence of centroid depth on the match between observed and synthetic waveforms. On each line, from left to right, we plot the (fixed) centroid depth (MMS is the minimum-misfit solution); the model *P* and *SH* focal spheres with each station plotted as its first letter in red (*P*) or green (*SH*), together with the model strike, dip, rake, and moment (Nm); the source time function; observed (red) and synthetic (black) *P* waveforms; and observed (green) and synthetic (black) *SH* waveforms.

To investigate this further, we ran a new set of body waveform models of the main shock earthquake in which all source parameters, including centroid depth, were set free. We varied the ambient, half-space seismic velocities between model runs and recorded the minimum-misfit centroid depth at each new choice of velocity. *P* wave velocities (V_p) were varied in 0.1 km/s steps between a lower bound of 4.5 km/s and an upper one of 6.5 km/s. *S* wave velocities (V_s) were calculated using the V_p/V_s ratio of 1.8, consistent with values determined in various nearby microseismic studies [*Hatzfeld et al.*, 2003; *Tatar et al.*, 2004; *Gholamzadeh et al.*, 2009; *Yaminifard et al.*, 2012a, 2012b].

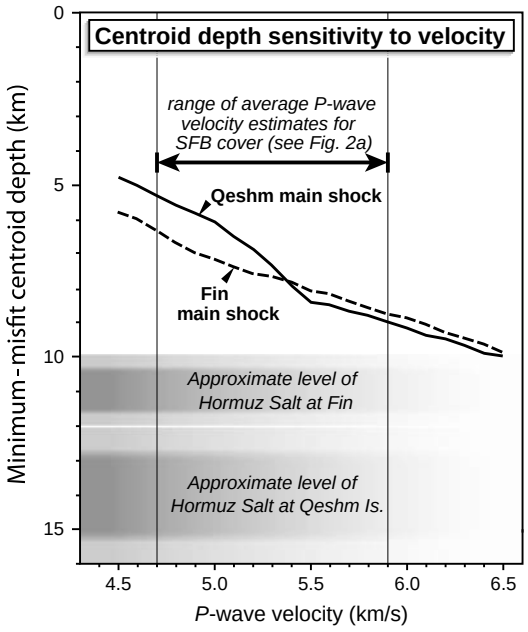

Figure 7. Minimum-misfit centroid depths for the 27 November 2005 Qeshm main shock (solid line) and the 25 March 2006 Fin main shock (dashed line) as a function of *P* wave velocity. We used a constant V_p/V_s ratio of 1.8.

Minimum-misfit centroid depths—plotted according to V_p as a solid line in Figure 7—vary between ~5 km (for V_p = 4.5 km/s) and ~10 km (for V_p = 6.5 km/s). Even at the highest end of this range, the centroid depth is wholly inconsistent with rupture centered at the same level as the microseismic aftershocks. In reality, the higher part of this range is anyway unrealistic, because microseismic experiments within the SFB all exhibit a narrower range in average cover *P* wave velocity of 4.7–5.7 km/s (Figure 2a and Figure 7).

The microseismic studies which detected the highest numbers of shallow events and which are therefore likely to have yielded the most accurate cover velocities—at Ghir [*Hatzfeld et al.*, 2003; *Tatar et al.*, 2004] and Masjed Soleyman [*Nissen et al.*,

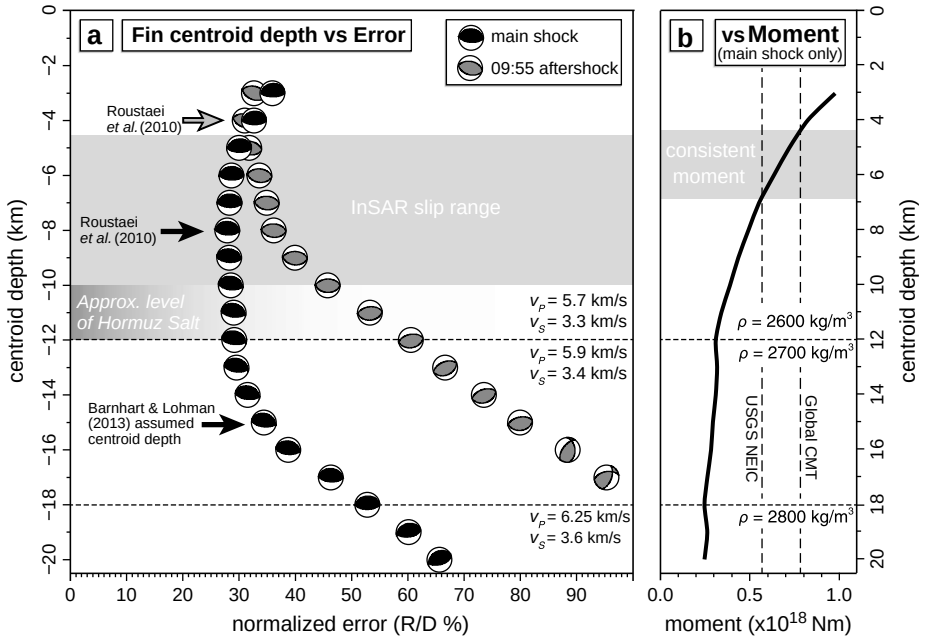

Figure 8. (a) Body waveform models of the 26 March 2006 Fin main shock (black) and its first major aftershock (grey), plotted as a function of their (fixed) centroid depths and normalized errors. We used the same velocity structure as *Roustaei et al.* [2010], shown on the right. The minimum-misfit, main shock centroid depth and the assumed depth of *Barnhart and Lohman* [2013] are picked out by black arrows, while the minimum-misfit aftershock centroid depth is marked by a grey arrow. The grey areas show the slip extents derived from InSAR [*Roustaei et al.*, 2010] and the estimated depth of the Hormuz salt in the onshore SE Fars Arc [e.g., *Sherkati et al.*, 2005]. (b) The black line shows the main shock body waveform model moment against depth. The assumed density structure is given on the right-hand side. Vertical lines show independent estimates of the moment from the GCMT catalog and the USGS National Earthquake Information Center (NEIC). The grey area highlights the depth range of body waveform models whose moment is consistent with these independent estimates.

2011]—exhibit cover *P* wave velocities of 4.7–5.0 km/s. This suggests that cover velocities determined by and used in the modeling of *Nissen et al.* [2010] and *Roustaei et al.* [2010] were too high, which in turn will have increased their centroid depths by ~1 km. The 4.7–5.0 km/s range in *P* wave velocities yields a centroid depth of 5–6 km, in close agreement with the central depth of the InSAR-derived models.

6.2. Fin Earthquakes

We repeated the body waveform experiments for the Fin main shock and 09:55 UTC aftershock, initially using the seismic velocities obtained by *Roustaei et al.* [2010]. The normalized error profile for the main shock (Figure 8a, black focal spheres) is much flatter than that for the Qeshm earthquakes, with a <10% increase in R/D over the centroid depth range 5–13 km. However, body waveform model moments are consistent with independent USGS NEIC and GCMT estimates over the much smaller range of ~5–7 km (Figure 8b). At a depth of 13 km, our model moment is ~80% smaller than the NEIC moment and ~250% smaller than the GCMT moment. At 15 km, there is a clear visual degradation to the fit of observed and synthetic *SH* waveforms, although *P* waveforms still produce a good match (Figure 6b). These results imply that the Fin main shock occurred within the midlower sedimentary cover; the 09:55 UTC aftershock probably ruptured the middle part of the cover, based on the well-defined trough in its normalized error profile (Figure 8a, grey focal spheres).

The effect of assumed seismic velocities on the main shock centroid depth is indicated by the dashed line in Figure 8. Over the realistic range of cover *P* wave velocities of 4.7–5.7 km/s, the centroid depth lies between ~6 km and ~9 km, in good agreement with the depth of the InSAR-derived model fault plane.

7. Discussion

7.1. Main Shock Depths

Our body waveform analyses confirm that the Qeshm and Fin main shocks, as well as their largest aftershocks, were centered within the middle sedimentary cover at depths which agree well with the

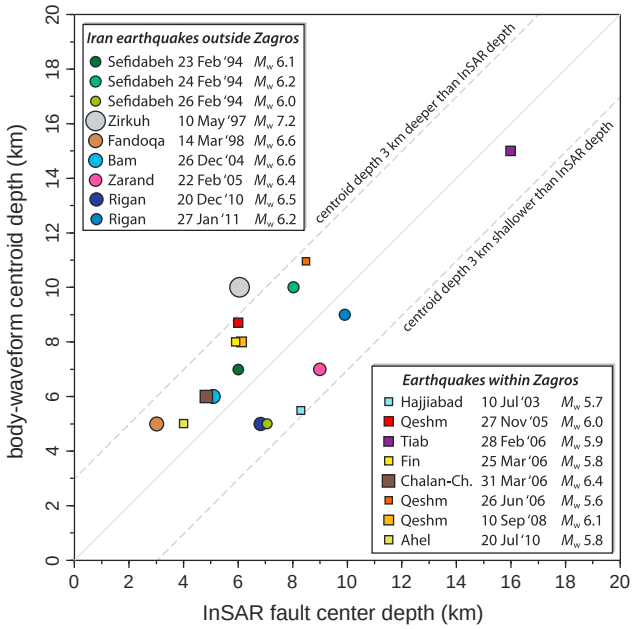

Figure 9. A plot of body waveform centroid depth against InSAR fault center depth for all earthquakes in Iran that have been modeled independently using both forms of data. Diagonal lines represent consistent depth estimates (solid) and ±3 km discrepancies (dashed). Squares show eight earthquakes from within the Zagros, and circles show nine earthquakes from other parts of Iran; all data points are scaled to earthquake magnitude. Data are from *Berberian et al.* [2000] and *Parsons et al.* [2006] (Sefidabeh), *Berberian et al.* [1999] and *Sudhaus and Jónsson* [2011] (Zirkuh), *Berberian et al.* [2001] (Fandoqa), *Adams et al.* [2009] and *Barnhart et al.* [2013] (Hajjiabad), *Funning et al.* [2005] and *Jackson et al.* [2006] (Bam), *Talebian et al.* [2006] (Zarand), *Nissen et al.* [2010] (Qeshm), *Nissen et al.* [2011] and *Barnhart et al.* [2013] (Tiab and Ahel), *Roustaei et al.* [2010] (Fin), *Peyret et al.* [2008] (Chalan-Chulan), and *Walker et al.* [2013] (Rigan).

InSAR-derived fault slip models. The "phantom earthquake" interpretation required that the minimum-misfit centroid depths were at least 6 km too deep, an error which is well beyond the limits suggested by other earthquake studies that incorporate both InSAR and body waveform analyses. For example, of the 17 earthquakes in Iran that have been modeled independently with InSAR and body waveforms, 14 yielded fault-center and centroid depths that agree to ±3 km (Figure 9). This close agreement includes all eight earthquakes studied using both techniques within the Zagros. Only the 1997 Zirkuh earthquake in eastern Iran shows a slightly larger difference of 4 km [*Berberian et al.*, 1999; *Sudhaus and Jónsson*, 2011], but this is easily the largest of these earthquakes and involved a complex, multisegment rupture that made assigning a centroid depth especially difficult. The close agreement in all other examples is striking given the assumptions inherent to both modeling approaches, particularly the simple velocity/elastic structure and the use of a point or planar source. These data strongly contradict the assertion of *Barnhart and Lohman* [2013] and *Barnhart et al.* [2013] that centroid depths obtained from careful analysis of teleseismic body waveforms are of little use in addressing these types of problems.

The difference between the depth of main shock slip and those of microseismic aftershocks at Qeshm and Fin is unequivocal but not entirely without precedent. We are aware of four other earthquake sequences which exhibit similar discrepancies. (1) The M_w 5.7 Potenza (Italy) earthquake of 1990 was assigned a centroid depth of ~11 km, but aftershock hypocenters were clustered within the depth range 15–25 km [*Azzara et al.*, 1993; *Ekström*, 1994]. (2) The M_w 6.8 Tottori (Japan) earthquake also involved shallow main shock slip, mostly above a depth of ~8 km, but subsequent aftershocks were concentrated at depths of 5–15 km with peak activity lying outside the principal main shock slip patch [*Semmane et al.*, 2005]. (3) A similar pattern was observed in the M_w 6.6 Bam (Iran) earthquake of 2005, with main shock slip focused at depths of ~1–11 km and aftershocks peaking at ~10–15 km [*Funning et al.*, 2005; *Tatar et al.*, 2005; *Jackson et al.*, 2006]. (Bam also lies close to Golbaf, where M_w 7.1 and M_s 6.6 earthquakes in 1981 and 1998, respectively, ruptured the same fault but were centered at significantly different depths [*Berberian et al.*, 2001]). (4) Major slip in the M_w 7.9 Wenchuan (China) earthquake of 2008 extended from the surface down to ~10 km, but most aftershocks occurred at depths of 8–20 km [*Tong et al.*, 2010].

Together with the Qeshm and Fin sequences, these indicate that the common practice of delimiting main shock fault planes from the distribution of aftershocks [e.g., *Das and Henry*, 2003] is not always applicable. It is also notable that in each case, main shock slip was shallower than most aftershocks. However, a unique aspect of the Qeshm and Fin sequences (compared to the other four examples) is the clear *separation* between main shock slip and aftershock microseismicity, there being no overlap between the two. There are really two separate attributes here: first, the absence of microseismicity on or around the main shock fault planes; second, the triggering of small earthquakes well below the main shock fault planes. We discuss these in turn, below.

7.2. Absence of Shallow Aftershock Microseismicity

An important point to note is that the absence of aftershock activity discussed here relates only to the duration of the local seismometer deployments, each beginning several days after the main shocks. Both Qeshm and Fin main shocks triggered teleseismically recorded aftershocks later on the same day. At Qeshm, M_w 5.0 and 5.4 aftershocks occurred within ~6 h of the main shock and a M_w 4.7 event was recorded teleseismically 3 days later [*Nissen et al.*, 2010]. At Fin, the main shock and four aftershocks of M_w 4.9–5.5 all occurred on the same day.

Local seismic networks are able to pinpoint earthquakes most accurately when they occur at depths which roughly correspond to the station spacing. The four stations deployed at Fin were spaced ~15–25 km apart and so the lack of shallow events here may partly reflect the poor resolution of the network at these depths. However, the 18 local seismometers deployed on Qeshm Island are spaced ~5–10 km apart, so the preponderance of deeper microearthquakes over those shallower than 10 km is robust. Genuinely shallow aftershocks should be easily identifiable by their small *S-P* times at close stations in the network, and none of these were detected.

Deficiencies in aftershock activity have been observed in a few other midsized continental earthquakes. The m_b 5.8 Ayers Rock (Australia) intraplate earthquake of 1989 is the most striking example: despite the installment of a local seismographic array with a detection threshold of M −1 to 0, not a single aftershock was detected [*Bowman et al.*, 1990]. The M_w 5.9 Galaxidi (Greece) earthquake of 1992 exhibited a near-complete lack of aftershocks close to its rupture plane; its largest aftershock was just M ~3.1 and within a week of the main shock seismicity had more-or-less returned to the background level [*Hatzfeld et al.*, 1996]. In this case, the earthquake was considered to have broken a strong barrier between two weaker fault segments upon which stresses were not sufficiently raised to induce aftershocks. In the Zagros examples, numerous weak layers within the thick sedimentary cover may have had a similar dampening effect on aftershock activity at the top and/or bottom of the main shock fault planes.

In all of these cases, the local network was installed several days after the initial earthquake (5 days at Galaxidi, 6 days at Ayers Rock, 9 days at Qeshm, and 19 days at Fin). This raises the possibility that early aftershocks *did* occur close to the fault plane but that by the time that seismometers were in place, activity had migrated away or disappeared altogether. Where dense seismic networks have captured earthquake-aftershock sequences in their entirety, it is not unusual to observe aftershock activity migrating away from the initial rupture planes [e.g., *Chiaraluce et al.*, 2003; *Toda and Stein*, 2003; *Chiarabba et al.*, 2009].

7.3. Deeper Aftershock Microseismicity and the Role of the Hormuz Salt

Although the aftershocks at Qeshm do not delineate an obvious fault structure, they do occur over a much narrower depth range than has been observed in other SFB microseismic experiments (Figure 2b). Two thirds of the hypocenters occurred between depths of 13 km and 16 km, agreeing closely with the estimated level of the Hormuz Fm in the SE coastal Fars Arc (*Jahani et al.* [2009] and section 6).

Halite becomes exponentially weaker with increasing temperature [e.g., *Franssen and Spiers*, 1990; *Marques et al.*, 2013], and at such depths and temperatures (probably ~200–400°C), the Hormuz salt itself is surely unable to host these aftershocks. However, the Hormuz salt is likely to flow along the basement-cover interface in response to coseismic strain of the overlying Competent Group sediments. As discussed in section 2.1, the weak halite is interbedded with a suite of other sediments which include anhydrites, limestones, and dolomites. Recent experiments on natural samples of these rock types indicate that they undergo a transition from velocity-strengthening to velocity-weakening behavior above ~150°C [*Verberne et al.*, 2010], while calcite gouge samples show stick-slip behavior at up to ~540°C (B. Verberne and C. Spiers, personal communication, 2013). These observations hint that anhydrite, dolomite, and limestone layers

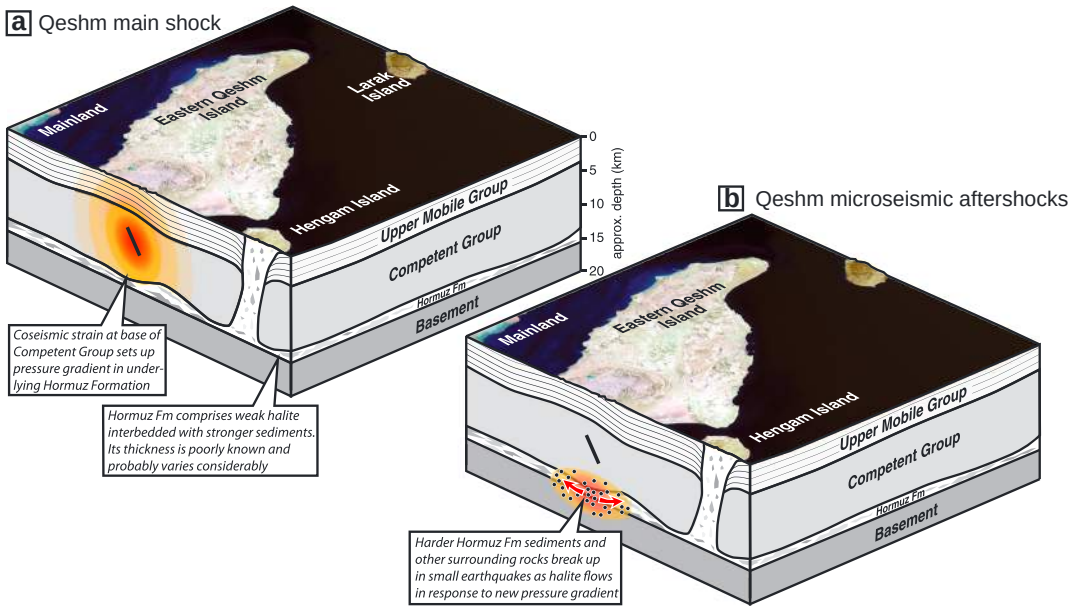

Figure 10. Schematic illustration of the Qeshm Island earthquake sequence. (a) The M_w ~6 main shock ruptures the Competent Group of sediments in the middle part of the cover (NB though we have drawn a S-dipping fault, the dip direction may equally be to the north). Strain at the base of the Competent Group causes a pressure gradient in the underlying Hormuz Formation. (b) Hormuz evaporites flow in response to this new pressure gradient. As they do so, interbedded dolomites and other harder sediments of the Hormuz Fm break up in small earthquakes.

with the Hormuz Fm may be the source of the observed microseismicity at Qeshm Island, as they fracture in response to the flow of the halite. Adjoining rocks must also be implicated if the observed aftershock depth range is to be reproduced, unless the Hormuz Fm is considerably thickened in this area. This scenario is shown schematically in Figure 10.

This mechanism of triggering accounts for the wholesale vertical separation of main shock slip and microseismic aftershocks, because the lowermost Competent Group sediments will strain considerably even though they do not rupture. As the resulting salt flow along the basement-cover interface is probably mostly horizontal, vertically oriented planes are most likely to slip, helping explain why strike-slip mechanisms are so predominant amongst the microseismic aftershocks. Small earthquakes induced by borehole injection of fluids along horizontal bedding are also mostly strike slip, with *P* axes oriented parallel to the regional direction of maximum horizontal compression [e.g., *Rutledge et al.*, 2004], much like the mechanisms obtained by *Yaminifard et al.* [2012a] at Qeshm. One issue which remains unclear is whether the flow of the Hormuz salt, triggered by the 2005 main shock, in turn helped trigger eight M_w 5–6 aftershocks which occurred between June 2006 and July 2009 (outside the time frame focused on in this paper). These events have shallow centroid depths of 4–11 km and so were probably also located within the cover [*Nissen et al.*, 2010]. However, it is difficult to address this question without much better constraints on the rheology and thickness of the Hormuz salt.

Last, it is worth noting that while we think the Hormuz salt plays an important role in the Qeshm and Fin earthquake sequences, evaporites cannot be implicated in all other cases where main shocks and aftershocks are vertically offset, such as at Bam and Golbaf in southeastern Iran [*Tatar et al.*, 2005; *Jackson et al.*, 2006; *Berberian et al.*, 2001].

7.4. Implications for Active Tectonics of the Zagros

Our careful scrutiny of the Qeshm and Fin earthquakes has important implications for the broad-scale tectonics of the Zagros Simply Folded Belt. *Nissen et al.* [2011] used centroid depths from numerous body waveform studies to suggest that most larger earthquakes in the SFB occur within the lower-to-middle parts of the sedimentary cover, rather than the basement as was previously thought (Figure 1c). However, some of these studies assumed half-space seismic velocities that are undoubtedly too fast: *Baker et al.* [1993] and *Maggi et al.* [2000] took V_p as 6.0 km/s and *Talebian and Jackson* [2004] used 6.5 km/s. Judging by Figure 7,

many of the centroid depths presented in these three papers are therefore ~1–3 km too deep. Correcting for this would have the effect of raising several of the earthquakes on Figure 1 from centroid depths which lie close to the basement-cover interface to ones which are unequivocally within the cover.

Most of these earthquakes are M_w5–6, with likely source dimensions of ~3–8 km. Given the 30–60° dips of most of the reverse faulting events, many of these earthquakes are probably contained entirely within the sedimentary cover, not only rupturing but also nucleating there. Large continental earthquakes usually nucleate within crystalline rocks [*Sibson*, 1982] and unequivocal examples of nucleation in carbonate sequences are quite rare [see *Scuderi et al.*, 2013]. The Zagros probably contains the best examples of this phenomenon, with the Qeshm and Fin earthquakes perhaps clearest of all. A few moderate magnitude events do occur beneath the Hormuz Fm, but shortening at basement depths is probably mostly aseismic [*Nissen et al.*, 2011; *Allen et al.*, 2013]. Nevertheless, microseismic activity at these depths is considerably more intense than within the sedimentary cover (Figure 2b).

Nissen et al. [2011] also pointed out a cutoff in earthquake magnitude in the SFB of around M_w ~6. In their view, the difficulty of transmitting stresses through the weak Hormuz salt effectively splits the seismogenic layer in two, helping to explain the large number of M_w5–6 earthquakes and the complete absence of any greater than M_w ~7 from both instrumental and historical records [*Nissen et al.*, 2011; *Ambraseys and Melville*, 1982]. Two M_w ~6.7 earthquakes—at Ghir (10 April 1972) and Khurgu (21 March 1977)—may complicate this simple view, as their larger source dimensions (coupled with the usual lack of surface rupturing) make them difficult to contain within the sedimentary cover alone. Local thinning of the Hormuz Fm and welding of Competent Group strata onto the underlying basement—as is observed in some of the reflection lines of [*Jahani et al.*, 2009]—may allow the Ghir and Khurgu-sized events to break through in some places more easily.

8. Conclusions

1. The Qeshm and Fin main shocks ruptured the middle part of the sedimentary cover and are vertically separated from deeper aftershock microseismicity. This casts doubt upon the practice of using aftershock distributions as a direct constraint on main shock slip extents regardless of tectonic setting.
2. There is no clear evidence to support large pulses of triggered, aseismic fault slip ("phantom earthquakes") in the sedimentary cover of the Simply Folded Belt.
3. At Qeshm, triggered microseismicity is centered at the estimated level of the Hormuz salt and may reflect breaking up of interbedded limestones, dolomites, and anhydrites and other neighboring strata as the halite flows in response to main shock strain at the base of the cover.
4. These results strongly support recent suggestions that the majority of moderate-large earthquakes within the Simply Folded Belt occur within the "Competent Group" of carbonate sediments that make up the middle and lower parts of the cover. These are perhaps the clearest examples of large earthquakes nucleating within a carbonate sequence anywhere in the world.
5. The Zagros basement, on the other hand, contains only rare moderate-large earthquakes, despite the preponderance of microseismicity at these depths. A few discrete basement faults—such as those implicated in the large Ghir and Khurgu earthquakes in the 1970s—may still play an important role in the tectonics of the SFB, but the basement probably shortens mostly aseismically.

Acknowledgments
This work is supported by the Natural Environmental Research Council through Earthquakes Without Frontiers (http://ewf.nerc.ac.uk/). Envisat ASAR data were provided by the European Space Agency and were processed using JPL/Caltech ROI-PAC software. Global Digital Seismographic Network (GDSN) data were obtained through the Incorporated Research Institute for Seismology (IRIS) Data Management Center. The seismic reflection lines in Figure 4 were kindly made available by the National Iranian Oil Company (NIOC). We appreciate informative discussions with Bill Barnhart, Eric Bergman, Alex Copley, Rowena Lohmann, Chris Spiers, and Bart Verberne. Finally, we are grateful to Frédéric Mouthereau and Gareth Funning for their careful reviews.

References

Adams, A., R. Brazier, A. Nyblade, A. Rodgers, and A. Al-Amri (2009), Source parameters for moderate earthquakes in the Zagros Mountains with implications for the depth extent of seismicity, *Bull. Seismol. Soc. Am.*, *99*, 2044–2049, doi:10.1785/0120080314.

Ala, M. A. (1974), Salt diapirism in Southern Iran, *AAPG Bull.*, *58*(1), 1758–1770.

Allen, M. B., and H. A. Armstrong (2008), Arabia Eurasia collision and the forcing of mid-Cenozoic global cooling, *Palaeogeogr. Palaeoclimatol. Palaeoecol.*, *265*, 52–58.

Allen, M. B., C. Saville, E. J.-P. Blanc, M. Talebian, and E. Nissen (2013), Orogenic plateau growth: Expansion of the Turkish-Iranian Plateau across the Zagros fold-and-thrust belt, *Tectonics*, *32*, 1–20, doi:10.1002/tect.20025.

Ambraseys, N. N., and C. P. Melville (1982), *A History of Persian Earthquakes*, Cambridge Univ. Press, Cambridge, U. K.

Azzara, R., A. Basili, L. Beranzoli, C. Chiarabba, R. Di Giovambattista, and G. Selvaggi (1993), The seismic sequence of Potenza (May 1990), *Ann. Geofis.*, *36*(1), 237–243.

Baker, C., J. Jackson, and K. Priestley (1993), Earthquakes on the Kazerun Line in the Zagros Mountains of Iran: Strike-slip faulting within a fold-and-thrust belt, *Geophys. J. Int.*, *115*, 41–61, doi:10.1111/j.1365-246X.1993.tb05587.x.

Barnhart, W. D., and R. B. Lohman (2012), Regional trends in active diapirism revealed by mountain range-scale InSAR time series, *Geophys. Res. Lett.*, *39*, L08309, doi:10.1029/2012GL051255.

Barnhart, W. D., and R. B. Lohman (2013), Phantom earthquakes and triggered aseismic creep: Vertical partitioning of strain during earthquake sequences in Iran, *Geophys. Res. Lett.*, *40*, 819–823, doi:10.1002/grl.50201.

Barnhart, W. D., R. B. Lohman, and R. J. Mellors (2013), Active accommodation of plate convergence in Southern Iran: Earthquake locations, triggered aseismic slip, and regional strain rates, *J. Geophys. Res. Solid Earth*, *118*, 5699–5711, doi:10.1002/jgrb.50380.

Berberian, M. (1995), Master blind thrust faults hidden under the Zagros folds: Active basement tectonics and surface morphotectonics, *Tectonophysics*, *241*, 193–224.

Berberian, M., and J. S. Tchalenko (1976), Earthquakes of Bandar Abbas-Hajiabad Region (Zagros, Iran), *Geol. Surv. Iran*, *39*, 371–396.

Berberian, M., J. A. Jackson, M. Qorashi, M. M. Khatib, K. Priestley, M. Talebian, and M. Ghafuri-Ashtiani (1999), The 1997 May 10 Zirkuh (Qa'enat) earthquake (M_w 7.2): Faulting along the Sistan suture zone of eastern Iran, *Geophys. J. Int.*, *136*, 671–694, doi:10.1046/j.1365-246x.1999.00762.x.

Berberian, M., J. A. Jackson, M. Qorashi, M. Talebian, M. Khatib, and K. Priestley (2000), The 1994 Sefidabeh earthquakes in eastern Iran: Blind thrusting and bedding-plane slip on a growing anticline, and active tectonics of the Sistan suture zone, *Geophys. J. Int.*, *142*, 283–299.

Berberian, M., J. A. Jackson, E. Fielding, B. E. Parsons, K. Priestley, M. Qorashi, M. Talebian, R. Walker, T. J. Wright, and C. Baker (2001), The 1998 March 14 Fandoqa earthquake (M_w 6.6) in Kerman province, southeast Iran: Re-rupture of the 1981 Sirch earthquake fault, triggering of slip on adjacent thrusts and the active tectonics of the Gowk fault zone, *Geophys. J. Int.*, *146*, 371–398, doi:10.1046/j.1365-246X.2001.01459.x.

Bie, L., I. Ryder, S. E. J. Nippress, and R. Bürgmann (2014), Coseismic and post-seismic activity associated with the 2008 Mw 6.3 Damxung earthquake, Tibet, constrained by InSAR, *Geophys. J. Int.*, *196*(2), 788–803, doi:10.1093/gji/ggt444.

Blanc, E. J.-P., M. B. Allen, S. Inger, and H. Hassani (2003), Structural styles in the Zagros Simple Folded Zone, Iran, *J. Geol. Soc. London*, *160*, 401–412, doi:10.1144/0016-764902-110.

Bowman, J. R., J. A. Collins, M. G. Bostock, J. Grant, and C. C. Bowman (1990), The Ayers Rock, Australia, earthquake of 28 May 1989: A temporally isolated mb 5.8 intraplate event, *Bull. Seismol. Soc. Am.*, *80*(2), 313–324.

Bürgmann, R., E. Fielding, and J. Sukhatme (1998), Slip along the Hayward fault, California, estimated from space-based synthetic aperture radar interferometry, *Geology*, *26*, 559–562.

Carruba, S., C. R. Perotti, R. Buonaguro, R. Calabrò, R. Carpi, and M. Naini (2006), Structural pattern of the Zagros fold-and-thrust belt in the Dezful Embayment (SW Iran), *Geol. S. Am. S.*, *414*, 11–32.

Casciello, E., J. Vergés, E. Saura, G. Casini, N. Fernández, E. Blanc, S. Homke, and D. W. Hunt (2009), Fold patterns and multilayer rheology of the Lurestan Province, Zagros Simply Folded Belt (Iran), *J. Geol. Soc. London*, *166*, 947–959.

Chiarabba, C., et al. (2009), The 2009 L'Aquila (Central Italy) M_W6.3 earthquake: Main shock and aftershocks, *Geophys. Res. Lett.*, *36*, L18308, doi:10.1029/2009GL039627.

Chiaraluce, L., W. L. Ellsworth, C. Chiarabba, and M. Cocco (2003), Imaging the complexity of an active normal fault system: The 1997 Colfiorito (Central Italy) case study, *J. Geophys. Res.*, *108*(B6), 2294, doi:10.1029/2002JB002166.

Chinnery, M. A., and D. B. Jovanovich (1972), Effect of Earth layering on earthquake displacement fields, *Bull. Seismol. Soc. Am.*, *62*(6), 1629–1639.

Colman-Sadd, S. P. (1978), Fold development in Zagros simply folded belt, Southwest Iran, *AAPG Bull.*, *62*, 984–1003.

Das, S., and C. Henry (2003), Spatial relation between main earthquake slip and its aftershock distribution, *Rev. Geophys.*, *41*, 1013, doi:10.1029/2002RG000119.

Deng, J., M. Gurnis, H. Kanamori, and E. Hauksson (1998), Viscoelastic flow in the lower crust after the 1992 Landers California, Earthquake, *Science*, *282*, 1689–1692, doi:10.1126/science.282.5394.1689.

Dubois, L., K. L. Feigl, D. Komatitsch, T. Árnadóttir, and F. Sigmundsson (2008), Three-dimensional mechanical models for the June 2000 earthquake sequence in the south Iceland seismic zone, *Tectonophysics*, *457*, 12–29, doi:10.1016/j.tecto.2008.05.020.

Edgell, H. S. (1996), Salt tectonism in the Persian Gulf Basin, *Geol. Soc. London Spec. Publ.*, *100*, 129–151, doi:10.1144/GSL.SP.1996.100.01.10.

Ekström, G. (1994), Teleseismic analysis of the 1990 and 1991 earthquakes near Potenza, *Ann. Geofis.*, *37*(6), 1591–1599.

Elliott, J. R., R. J. Walters, P. C. England, J. A. Jackson, Z. Li, and B. Parsons (2010), Extension on the Tibetan plateau: Recent normal faulting measured by InSAR and body wave seismology, *Geophys. J. Int.*, *183*, 503–535, doi:10.1111/j.1365-246X.2010.04754.x.

Elliott, J. R., B. Parsons, J. A. Jackson, X. Shan, R. A. Sloan, and R. T. Walker (2011), Depth segmentation of the seismogenic continental crust: The 2008 and 2009 Qaidam earthquakes, *Geophys. Res. Lett.*, *38*, L06305, doi:10.1029/2011GL046897.

Emmerson, B., J. Jackson, D. McKenzie, and K. Priestley (2006), Seismicity, structure and rheology of the lithosphere in the Lake Baikal region, *Geophys. J. Int.*, *167*, 1233–1272, doi:10.1111/j.1365-246X.2006.03075.x.

Engdahl, E. R., R. D. van der Hilst, and R. Buland (1998), Global teleseismic earthquake relocation from improved travel times and procedures for depth determination, *Bull. Seismol. Soc. Am.*, *88*, 722–743.

Engdahl, R. E., J. A. Jackson, S. C. Myers, E. A. Bergman, and K. Priestley (2006), Relocation and assessment of seismicity in the Iran region, *Geophys. J. Int.*, *167*, 761–778, doi:10.1111/j.1365-246X.2006.03127.x.

Fakhari, M. D., G. J. Axen, B. K. Horton, J. Hassanzadeh, and A. Amini (2008), Revised age of proximal deposits in the Zagros foreland basin and implications for Cenozoic evolution of the High Zagros, *Tectonophysics*, *451*, 170–185.

Fox, B. D., N. D. Selby, R. Heyburn, and J. H. Woodhouse (2012), Shallow seismic source parameter determination using intermediate-period surface wave amplitude spectra, *Geophys. J. Int.*, *191*, 601–615, doi:10.1111/j.1365-246X.2012.05612.x.

Franssen, R. C. M. W., and C. J. Spiers (1990), Deformation of polycrystalline salt in compression and in shear at 250–350°C, *Geol. Soc. London Spec. Publ.*, *54*, 201–213, doi:10.1144/GSL.SP.1990.054.01.20.

Fredrich, J., R. McCaffrey, and D. Denham (1988), Source parameters of seven large Australian earthquakes determined by body waveform inversion, *Geophys. J. Int.*, *95*, 1–13, doi:10.1111/j.1365-246X.1988.tb00446.x.

Funning, G. J., B. Parsons, T. J. Wright, J. A. Jackson, and E. J. Fielding (2005), Surface displacements and source parameters of the 2003 Bam (Iran) earthquake from Envisat advanced synthetic aperture radar imagery, *J. Geophys. Res.*, *110*, B09406, doi:10.1029/2004JB003338.

Futterman, W. I. (1962), Dispersive body waves, *J. Geophys. Res.*, *67*, 5279–5291, doi:10.1029/JZ067i013p05279.

Gansser, A. (1960), Uber Schlammvulkane und Salzdome, *Vjschr. Naturf. Ges. Zurich.*, *105*, 1–46.

Gercek, H. (2007), Poisson's ratio values for rocks, *Int. J. Rock Mech. Min. Sci.*, *44*(1), 1–13.

Gholamzadeh, A., F. Yamini-Fard, K. Hessami, and M. Tatar (2009), The February 28, 2006 Tiab earthquake, M_W 6.0: Implications for tectonics of the transition between the Zagros continental collision and the Makran subduction zone, *J. Geodyn.*, *47*, 280–287, doi:10.1016/j.jog.2009.01.005.

Hatzfeld, D., et al. (1996), The Galaxidi earthquake of 18 November 1992: A possible asperity within the normal fault system of the Gulf of Corinth (Greece), *Bull. Seismol. Soc. Am.*, *86*(6), 1987–1991.
Hatzfeld, D., M. Tatar, K. Priestley, and M. Ghafory-Ashtiany (2003), Seismological constraints on the crustal structure beneath the Zagros Mountain belt (Iran), *Geophys. J. Int.*, *155*(2), 403–410, doi:10.1046/j.1365-246X.2003.02045.x.
Hearn, E. H., and R. Bürgmann (2005), The effect of elastic layering on inversions of GPS data for coseismic slip and resulting stress changes: Strike-slip earthquakes, *Bull. Seismol. Soc. Am.*, *95*(5), 1637–1653.
Hessami, K., H. A. Koyi, C. J. Talbot, H. Tabasi, and E. Shabanian (2001), Progressive unconformities within an evolving foreland fold thrust belt, Zagros Mountains, *J. Geol. Soc. London*, *158*, 969–981.
Hessami, K., F. Nilforoushan, and C. J. Talbot (2006), Active deformation within the Zagros Mountains deduced from GPS measurements, *J. Geol. Soc. London*, *163*(1), 143–148.
Jackson, J., and T. Fitch (1981), Basement faulting and the focal depths of the larger earthquakes in the Zagros mountains (Iran), *Geophys. J. Int.*, *64*, 561–586, doi:10.1111/j.1365-246X.1981.tb02685.x.
Jackson, J., and D. McKenzie (1984), Active tectonics of the Alpine-Himalayan Belt between western Turkey and Pakistan, *Geophys. J. Int.*, *77*, 185–264, doi:10.1111/j.1365-246X.1984.tb01931.x.
Jackson, J., and D. McKenzie (1988), The relationship between plate motions and seismic moment tensors, and the rates of active deformation in the Mediterranean and Middle East, *Geophys. J. Int.*, *93*, 45–73, doi:10.1111/j.1365-246X.1988.tb01387.x.
Jackson, J., et al. (2006), Seismotectonic, rupture process, and earthquake-hazard aspects of the 2003 December 26 Bam, Iran, earthquake, *Geophys. J. Int.*, *166*, 1270–1292.
Jackson, J. A. (1980), Reactivation of basement faults and crustal shortening in orogenic belts, *Nature*, *283*, 343–346, doi:10.1038/283343a0.
Jahani, S. (2008), Tectonique salifè, replissement et fracturation dans les provinces du Fars Oriental et le domaine marin adjacent du Golfe Persique (Iran), PhD thesis, Université de Cergy-Pontoise.
Jahani, S., J.-P. Callot, D. Frizon de Lamotte, J. Letouzey, and P. Leturmy (2007), The salt diapirs of the eastern Fars province (Zagros, Iran): A brief outline of their past and present, in *Thrust Belts and Foreland Basins*, edited by O. Lacombe et al., pp. 289–308, Springer, Berlin Heidelberg, doi:10.1007/978-3-540-69426-7.
Jahani, S., J.-P. Callot, J. Letouzey, and D. Frizon de Lamotte (2009), The eastern termination of the Zagros Fold-and-Thrust Belt, Iran: Structures, evolution, and relationships between salt plugs, folding, and faulting, *Tectonics*, *28*, TC6004, doi:10.1029/2008TC002418.
James, G. A., and J. G. Wynd (1965), Stratigraphic nomenclature of Iranian oil consortium agreement area, *AAPG Bull.*, *49*, 2182–2245.
Kadinsky-Cade, K., and M. Barazangi (1982), Seismotectonics of southern Iran: The Oman line, *Tectonics*, *1*, 389–412, doi:10.1029/TC001i005p00389.
Kao, H., and W.-P. Chen (2000), The Chi-Chi earthquake sequence: Active, out-of-sequence thrust faulting in Taiwan, *Science*, *288*, 2346–2349, doi:10.1126/science.288.5475.2346.
Kent, P. E. (1970), The salt plugs of the Persian Gulf Region, *J. Petrol. Geol.*, *64*, 55–88.
Kent, P. E. (1979), The emergent Hormuz salt plugs of southern Iran, *J. Petrol. Geol.*, *2*, 117–144.
Khadivi, S., F. Mouthereau, J.-C. Larrasoaña, J. Vergés, O. Lacombe, E. Khademi, E. Beamud, M. Melinte-Dobrinescu, and J.-P. Suc (2010), Magnetochronology of synorogenic Miocene foreland sediments in the Fars arc of the Zagros Folded Belt (SW Iran), *Basin Res.*, *22*, 918–932, doi:10.1111/j.1365-2117.2009.00446.x.
Langston, C. A., and D. V. Helmberger (1975), A Procedure for modelling shallow dislocation sources, *Geophys. J. R. Astron. Soc.*, *42*(1), 117–130.
Lohman, R. B., and W. D. Barnhart (2010), Evaluation of earthquake triggering during the 2005–2008 earthquake sequence on Qeshm Island, Iran, *J. Geophys. Res.*, *115*, B12413, doi:10.1029/2010JB007710.
Lohman, R. B., M. Simons, and B. Savage (2002), Location and mechanism of the Little Skull Mountain earthquake as constrained by satellite radar interferometry and seismic waveform modeling, *J. Geophys. Res.*, *107*(B6), 2118, doi:10.1029/2001JB000627.
Maggi, A., J. A. Jackson, K. Priestley, and C. Baker (2000), A re-assessment of focal depth distributions in southern Iran, the Tien Shan and northern India: Do earthquakes really occur in the continental mantle?, *Geophys. J. Int.*, *143*, 629–661, doi:10.1046/j.1365-246X.2000.00254.x.
Marques, F. O., J.-P. Burg, M. Armann, and E. Martinho (2013), Rheology of synthetic polycrystalline halite in torsion, *Tectonophysics*, *583*, 124–130, doi:10.1016/j.tecto.2012.10.024.
Masson, F., J. Chèry, D. Hatzfeld, J. Martinod, P. Vernant, F. Tavakoli, and M. Ghafory-Ashtiani (2005), Seismic versus aseismic deformation in Iran inferred from earthquakes and geodetic data, *Geophys. J. Int.*, *160*, 217–226, doi:10.1111/j.1365-246X.2004.02465.x.
Massonnet, D., and K. L. Feigl (1995), Satellite radar interferometric map of the coseismic deformation field of the M = 6.1 Eureka Valley, California Earthquake of May 17, 1993, *Geophys. Res. Lett.*, *22*, 1541–1544, doi:10.1029/95GL01088.
Massonnet, D., K. Feigl, M. Rossi, and F. Adragna (1994), Radar interferometric mapping of deformation in the year after the Landers earthquake, *Nature*, *369*, 227–230, doi:10.1038/369227a0.
McCaffrey, R., and G. Abers (1988), SYN3: A program for inversion of teleseismic body wave forms on microcomputers, *Air Force Geophysical Laboratory Technical Report*, Hanscomb Air Force Base, Mass.
McCaffrey, R., P. Zwick, and G. Abers (1991), SYN4 Program, *Tech. Rep.*, IASPEI Software Library.
McQuarrie, N. (2004), Crustal scale geometry of the Zagros fold-thrust belt, Iran, *J. Struct. Geol.*, *26*, 519–535.
McQuarrie, N., and D. J. J. van Hinsbergen (2013), Retrodeforming the Arabia-Eurasia collision zone: Age of collision versus magnitude of continental subduction, *Geology*, *41*(3), 315–318.
Molinaro, M., J.-C. Guezou, P. Leturmy, S. A. Eshraghi, and D. Frizon de Lamotte (2004), The origin of changes in structural style across the Bandar Abbas syntaxis, SE Zagros (Iran), *Mar. Pet. Geol.*, *21*, 735–752.
Molinaro, M., P. Leturmy, J.-C. Guezou, D. Frizon de Lamotte, and S. A. Eshraghi (2005), The structure and kinematics of the southeastern Zagros fold-thrust belt, Iran: From thin-skinned to thick-skinned tectonics, *Tectonics*, *24*, TC3007, doi:10.1029/2004TC001633.
Molnar, P., and H. Lyon-Caen (1989), Fault plane solutions of earthquakes and active tectonics of the Tibetan Plateau and its margins, *Geophys. J. Int.*, *99*, 123–154, doi:10.1111/j.1365-246X.1989.tb02020.x.
Mouthereau, F. (2011), Timing of uplift in the Zagros belt/Iranian plateau and accommodation of late Cenozoic Arabia-Eurasia convergence, *Geol. Mag.*, *148*, 726–738.
Mouthereau, F., O. Lacombe, and J. Vergés (2012), Building the Zagros collisional orogen: Timing, strain distribution and the dynamics of Arabia/Eurasia plate convergence, *Tectonophysics*, *532*, 27–60.
Ni, J., and M. Barazangi (1986), Seismotectonics of the Zagros continental collision zone and a comparison with the Himalayas, *J. Geophys. Res.*, *91*, 8205–8218, doi:10.1029/JB091iB08p08205.

Nissen, E., B. Emmerson, G. J. Funning, A. Mistrukov, B. Parsons, D. P. Robinson, E. Rogozhin, and T. J. Wright (2007a), Combining InSAR and seismology to study the 2003 Siberian Altai earthquakes-dextral strike-slip and anticlockwise rotations in the northern India-Eurasia collision zone, *Geophys. J. Int.*, *169*, 216–232, doi:10.1111/j.1365-246X.2006.03286.x.

Nissen, E., M. Ghorashi, J. Jackson, P. Parsons, and M. Talebian (2007b), The 2005 Qeshm Island earthquake (Iran)—A link between buried reverse faulting and surface folding in the Zagros Simply Folded Belt?, *Geophys. J. Int.*, *171*, 326–338, doi:10.1111/j.1365-246X.2007.03514.x.

Nissen, E., F. Yamini-Fard, M. Tatar, A. Gholamzadeh, E. Bergman, J. R. Elliott, J. A. Jackson, and B. Parsons (2010), The vertical separation of mainshock rupture and microseismicity at Qeshm island in the Zagros Simply Folded Belt, Iran, *Earth Planet. Sci. Lett.*, *296*, 181–194.

Nissen, E., M. Tatar, J. A. Jackson, and M. B. Allen (2011), New views on earthquake faulting in the Zagros fold-and-thrust belt of Iran, *Geophys. J. Int.*, *186*, 928–944.

O'Brien, C. A. E. (1957), Salt diapirism in south Persia, *Geol. Mijnbouw*, *19*, 357–376.

Okada, Y. (1985), Surface deformation due to shear and tensile faults in a half-space, *Bull. Seismol. Soc. Am.*, *75*, 1135–1154.

Parsons, B., T. Wright, P. Rowe, J. Andrews, J. Jackson, R. Walker, M. Khatib, M. Talebian, E. Bergman, and E. R. Engdahl (2006), The 1994 Sefidabeh (eastern Iran) earthquakes revisited: New evidence from satellite radar interferometry and carbonate dating about the growth of an active fold above a blind thrust fault, *Geophys. J. Int.*, *164*, 202–217, doi:10.1111/j.1365-246X.2005.02655.x.

Peltzer, G., P. Rosen, F. Rogez, and K. Hudnut (1996), Postseismic rebound in fault step-overs caused by pore fluid flow, *Science*, *273*, 1202–1204, doi:10.1126/science.273.5279.1202.

Peyret, M., F. Rolandone, S. Dominguez, Y. Djamour, and B. Meyer (2008), Source model for the Mw 6.1, 31 March 2006, Chalan-Chulan Earthquake (Iran) from InSAR, *Terra Nova*, *20*, 126–133.

Pollitz, F. F. (1996), Coseismic deformation from earthquake faulting on a layered spherical Earth, *Geophys. J. Int.*, *125*(1), 1–14.

Priestley, K., C. Baker, and J. Jackson (1994), Implications of earthquake focal mechanism data for the active tectonics of the south Caspian Basin and surrounding regions, *Geophys. J. Int.*, *118*, 111–141, doi:10.1111/j.1365-246X.1994.tb04679.x.

Roustaei, M., E. Nissen, M. Abbassi, A. Gholamzadeh, M. Ghorashi, M. Tatar, F. Yamini-Fard, E. Bergman, J. Jackson, and B. Parsons (2010), The 25 March 2006 Fin earthquakes (Iran)—Insights into the vertical extents of faulting in the Zagros Simply Folded Belt, *Geophys. J. Int.*, *181*, 1275–1291, doi:10.1111/j.1365-246X.2010.04601.x.

Rutledge, J. T., W. S. Phillips, and M. J. Mayerhofer (2004), Faulting induced by forced fluid injection and fluid flow forced by faulting: An interpretation of hydraulic-fracture microseismicity, Carthage Cotton Valley Gas Field, Texas, *Bull. Seismol. Soc. Am.*, *94*, 1817–1830, doi:10.1785/012003257.

Savage, J. C. (1987), Effect of crustal layering upon dislocation modeling, *J. Geophys. Res.*, *92*, 10,595–10,600, doi:10.1029/JB092iB10p10595.

Scholz, C. (1990), *The Mechanics of Earthquakes and Faulting*, Cambridge Univ. Press, Cambridge, U. K.

Scuderi, M. M., A. R. Niemeijer, C. Collettini, and C. Marone (2013), Frictional properties and slip stability of active faults within carbonate-evaporite sequences: The role of dolomite and anhydrite, *Earth Planet. Sci. Lett.*, *369*, 220–232.

Semmane, F., F. Cotton, and M. Campillo (2005), The 2000 Tottori earthquake: A shallow earthquake with no surface rupture and slip properties controlled by depth, *J. Geophys. Res.*, *110*, B03306, doi:10.1029/2004JB003194.

Sepehr, M., J. Cosgrove, and M. Moieni (2006), The impact of cover rock rheology on the style of folding in the Zagros fold-thrust belt, *Tectonophysics*, *427*, 265–281, doi:10.1016/j.tecto.2006.05.021.

Sherkati, S., and J. Letouzey (2004), Variation of structural style and basin evolution in the central Zagros (Izeh zone and Dezful Embayment), Iran, *Mar. Petrol. Geol.*, *21*, 535–554.

Sherkati, S., M. Molinaro, D. Frizon de Lamotte, and J. Letouzey (2005), Detachment folding in the Central and Eastern Zagros fold-belt (Iran): Salt mobility, multiple detachments and late basement control, *J. Struct. Geol.*, *27*, 1680–1696, doi:10.1016/j.jsg.2005.05.010.

Sibson, R. H. (1982), Fault zone models, heat flow, and the depth distribution of earthquakes in the continental crust of the United States, *Bull. Seismol. Soc. Am.*, *72*(1), 151–163.

Sudhaus, H., and S. Jónsson (2011), Source model for the 1997 Zirkuh earthquake (M_W= 7.2) in Iran derived from JERS and ERS InSAR observations, *Geophys. J. Int.*, *185*, 676–692, doi:10.1111/j.1365-246X.2011.04973.x.

Talebian, M., and J. Jackson (2004), A reappraisal of earthquake focal mechanisms and active shortening in the Zagros mountains of Iran, *Geophys. J. Int.*, *156*, 506–526, doi:10.1111/j.1365-246X.2004.02092.x.

Talebian, M., et al. (2006), The Dahuiyeh (Zarand) earthquake of 2005 February 22 in central Iran: Reactivation of an intramountain reverse fault, *Geophys. J. Int.*, *164*, 137–148, doi:10.1111/j.1365-246X.2005.02839.x.

Tatar, M., D. Hatzfeld, and M. Ghafory-Ashtiany (2004), Tectonics of the Central Zagros (Iran) deduced from microearthquake seismicity, *Geophys. J. Int.*, *156*, 255–266, doi:10.1111/j.1365-246X.2003.02145.x.

Tatar, M., D. Hatzfeld, A. S. Moradi, and A. Paul (2005), The 2003 December 26 Bam earthquake (Iran), Mw 6.6, aftershock sequence, *Geophys. J. Int.*, *163*, 90–105, doi:10.1111/j.1365-246X.2005.02639.x.

Taymaz, T., J. Jackson, and R. Westaway (1990), Earthquake mechanisms in the Hellenic Trench near Crete, *Geophys. J. Int.*, *102*, 695–731, doi:10.1111/j.1365-246X.1990.tb04590.x.

Toda, S., and R. Stein (2003), Toggling of seismicity by the 1997 Kagoshima earthquake couplet: A demonstration of time-dependent stress transfer, *J. Geophys. Res.*, *108*(B12), 2567, doi:10.1029/2003JB002527.

Tong, X., D. T. Sandwell, and Y. Fialko (2010), Coseismic slip model of the 2008 Wenchuan earthquake derived from joint inversion of interferometric synthetic aperture radar, GPS, and field data, *J. Geophys. Res.*, *115*, B04314, doi:10.1029/2009JB006625.

Trasatti, E., C. Kyriakopoulos, and M. Chini (2011), Finite element inversion of DInSAR data from the Mw 6.3 L'Aquila earthquake, 2009 (Italy), *Geophys. Res. Lett.*, *38*, L08306, doi:10.1029/2011GL046714.

Verberne, B. A., C. He, and C. J. Spiers (2010), Frictional properties of sedimentary rocks and natural fault gouge from the Longmen Shan Fault Zone, Sichuan, China, *Bull. Seismol. Soc. Am.*, *100*, 2767–2790, doi:10.1785/0120090287.

Vergès, J., M. G. H. Goodarzi, H. Emami, R. Karpuz, J. Efstathiou, and P. Gillespie (2011), Multiple detachment folding in Pusht-e Kuh arc, Zagros: Role of mechanical stratigraphy, in *Thrust fault related folding*, edited by K. McClay, J. H. Shaw, and J. Suppe, pp. 69–94, Amer. Assoc. Petrol. Geol. Mem. 94, Tulsa, Okla.

Walker, R. T., L. A. Ramsey, and J. Jackson (2011), Geomorphic evidence for ancestral drainage patterns in the Zagros Simple Folded Zone and growth of the Iranian plateau, *Geol. Mag.*, *148*(5–6), 901–910.

Walker, R. T., et al. (2013), The 2010-2011 South Rigan (Baluchestan) earthquake sequence and its implications for distributed deformation and earthquake hazard in southeast Iran, *Geophys. J. Int.*, *193*, 349–374, doi:10.1093/gji/ggs109.

Walpersdorf, A., D. Hatzfeld, H. Nankali, F. Tavakoli, F. Nilforoushan, M. Tatar, P. Vernant, J. Chèry, and F. Masson (2006), Difference in the GPS deformation pattern of North and Central Zagros (Iran), *Geophys. J. Int.*, *167*, 1077–1088, doi:10.1111/j.1365-246X.2006.03147.x.

Weston, J., A. M. G. Ferreira, and G. J. Funning (2011), Global compilation of interferometric synthetic aperture radar earthquake source models: 1. Comparisons with seismic catalogs, *J. Geophys. Res.*, *116*, B08408, doi:10.1029/2010JB008131.

Weston, J., A. M. G. Ferreira, and G. J. Funning (2012), Systematic comparisons of earthquake source models determined using InSAR and seismic data, *Tectonophysics*, *532*, 61–81, doi:10.1016/j.tecto.2012.02.001.

Wright, T., B. Parsons, and E. Fielding (2001), Measurement of interseismic strain accumulation across the North Anatolian Fault by satellite radar interferometry, *Geophys. Res. Lett.*, *28*, 2117–2120, doi:10.1029/2000GL012850.

Wright, T. J., J. R. Elliott, H. Wang, and I. Ryder (2013), Earthquake cycle deformation and the Moho: Implications for the rheology of continental lithosphere, *Tectonophysics*, *609*, 504–523, doi:10.1016/j.tecto.2013.07.029.

Yamato, P., B. J. P. Kaus, F. Mouthereau, and S. Castelltort (2011), Dynamic constraints on the crustal-scale rheology of the Zagros fold belt, Iran, *Geology*, *39*(9), 815–818.

Yaminifard, F., M. Hassanpour Sedghi, A. Gholamzadeh, M. Tatar, and K. Hessami (2012a), Aftershock analysis of the 2005 November 27 (Mw 5.8) Qeshm Island earthquake (Zagros-Iran): Triggering of strike-slip faults at the basement, *J. Geodyn.*, *55*, 56–65.

Yaminifard, F., M. Tatar, K. Hessami, A. Gholamzadeh, and E. A. Bergman (2012b), Aftershock analysis of the 2005 November 27 (Mw 5.8) Qeshm Island earthquake (Zagros-Iran): Triggering of strike-slip faults at the basement, *J. Geodyn.*, *61*, 138–147.

Zwick, P., R. McCaffrey, and G. Abers (1994), MT5 Program, *IASPEI Software Library 4*.